nature neuroscience

Article

https://doi.org/10.1038/s41593-026-02239-7

The neurovascular impulse response function differentially reflects intrinsic neuromodulation across cortical regions

Received: 3 October 2024

Accepted: 11 February 2026

Bradley C. Rauscher[1,17], Natalie Fomin-Thunemann[2,17], Sreekanth Kura[2], Patrick R. Doran[1], Pablo D. Perez[2], Kıvılcım Kılıç[2], Emily A. Martin[3], Dora Balog[1], Nathan X. Chai[4], Francesca A. Froio[4], Patrick F. Bloniasz[5], Kate E. Herrema[1], Rockwell P. Tang[1], Scott G. Knudstrup[3], Andrew Garcia[6], John X. Jiang[2], Jeffrey P. Gavornik[7], Michael London[8], David Kleinfeld[9,10], Michael E. Hasselmo[11], Laura D. Lewis[12,13], Sava Sakadzic[12], Lei Tian[2,14], Gal Mishne[15], Emily P. Stephen[16], Martin Thunemann[2], David A. Boas[2] & Anna Devor[2,12] ✉

Neuromodulatory transmitters have vasoactive properties. Therefore, the impulse response function (IRF) linking spontaneous neuronal activity with hemodynamics may depend on neuromodulation. To test this hypothesis, we used optical imaging to measure norepinephrine (NE) or acetylcholine (ACh), calcium (Ca^{2+}) activity of cortical neurons and hemodynamics in cerebral cortex in awake mice. We show that modeling of hemodynamics as a weighted sum of Ca^{2+}-specific and NE-specific IRFs (IRF_{Ca2+} and IRF_{NE}) convolved with the respective time courses dramatically improved the model performance compared to using IRF_{Ca2+} alone. In contrast to NE, ACh was largely redundant with Ca^{2+} and, therefore, did not improve the hemodynamic estimation. Because NE covaried with arousal, we observed instances of the diminished hemodynamic coherence between cortical regions during high arousal despite coherent behavior of the underlying neuronal Ca^{2+} activity. We conclude that, without accounting for noradrenergic neuromodulation, diminished hemodynamic coherence can be falsely interpreted as neuronal desynchronizations in neuroimaging studies.

Ascending adrenergic and cholinergic projections from the locus coeruleus (LC) and basal forebrain (BF) have long been associated with shaping information processing in local and large-scale cortical networks[1,2] and modulation of cognitive functions such as arousal and attention[3]. The respective neurotransmitters, norepinephrine (NE) and acetylcholine (ACh), are vasoactive affecting cerebral blood flow (CBF) in two ways: directly, by acting on smooth muscle of arterioles, and indirectly, through modulation of local neurons[4,5]. These neuromodulatory systems are active in any conscious human subject participating in a blood-oxygenation-level-dependent (BOLD) functional magnetic resonance imaging (fMRI) study. Yet, how these systems affect the relationship between activity of local neuronal circuits and hemodynamics across cortical regions remains unclear.

Optogenetic (OG), chemogenetic and pharmacological perturbations of NE and ACh signaling in animals produce widespread hemodynamic changes and modulate the temporal correlation of hemodynamics across brain regions (that is, functional connectivity, FC)[6–13]. Complementary to the perturbation approach, it is now possible to directly visualize release of neuromodulatory transmitters in cerebral cortex in vivo thanks to the recent development of genetically encoded optical biosensors[14–17] and wide-field, large-scale 'mesoscopic' optical imaging[18–20].

A full list of affiliations appears at the end of the paper. ✉e-mail: adevor@bu.edu

In the present study, we leveraged our version of a wide-field mesoscope[18], along with two-photon microscopy, to assess the relationship between Ca^{2+} activity of cortical neurons and the associated hemodynamics during spontaneous activity in fully awake mice. We show that, while this relationship varied across cortical regions and NE levels, hemodynamic fluctuations were accurately predicted given the local Ca^{2+} and NE signals. In particular, the impulse response function (IRF) linking neuronal Ca^{2+} activity with hemodynamics was modulated by NE and the state of arousal in the anterior dorsal cortex. This effect resulted in diminished hemodynamic coherence between this region and several primary somatosensory areas despite an increase in coherence of the underlying neuronal Ca^{2+} activity.

Results

Neurovascular coupling depends on neuromodulation and behavior

We used mesoscopic imaging to simultaneously measure Ca^{2+}, hemodynamics (oxyhemoglobin, deoxyhemoglobin and total hemoglobin, HbO/HbR/HbT) and release of a neuromodulatory transmitter (NE or ACh) over the dorsal cortical surface in fully awake mice (Fig. 1a,b, Supplementary Video 1 and Methods). First, we focused on the relationship between Ca^{2+} as a measure of local neuronal activity and HbT as a measure reflecting vasodilation and vasoconstriction (under the assumption of constant hematocrit). Applying a classical hemodynamic response model, where a global (stationary in space and time) IRF (Methods) is convolved with the neuronal variable (Ca^{2+}) to return the hemodynamic variable (HbT), produced poor results (Fig. 1c and Extended Data Fig. 1a). Estimating the IRF for the medial part of the somatosensory regions of interest (ROIs), where the model's performance was better compared to other regions, further improved the fit for that ROI but at the cost of reduced accuracy elsewhere (Fig. 1d and Extended Data Fig. 1b). Relaxing the spatial homogeneity constraint of the convolution kernel and allowing the individual alpha function weights (*A* and *B* in Eq. 2; Methods) to vary pixel by pixel produced a modest improvement (Fig. 1e,f and Extended Data Fig. 1c).

Next, we asked whether the accuracy of the convolution model varied in time, potentially reflecting spontaneous neuromodulation dynamics (Supplementary Video 2). In Fig. 1g, we plot the model performance, evaluated within a 15-s sliding time window, against simultaneously imaged NE in one subject. Indeed, the model performance decreased with an increase in the level of NE (Fig. 1g and Supplementary Video 2). In particular, this inverse correlation was observed in the anterior dorsal cortex and, to a lesser extent, in the barrel cortex (Fig. 1g–i). Consistent with previous reports and known role of NE in arousal[21], the level of NE had high correlation with the eye pupil diameter (Supplementary Videos 1 and 2 and Extended Data Fig. 2c). Thus, the model performance decreased with an increase in arousal.

Because mice in this study expressed either $GRAB_{NE}$ or $GRAB_{ACh}$, the analysis with respect to NE and ACh was performed in a different group of subjects. In contrast to NE, ACh consistently covaried with low-pass-filtered Ca^{2+} (<0.5 Hz). Compared to NE, ACh and (low-pass-filtered) Ca^{2+} had higher correlation (ACh, $r = 0.70 \pm 0.03$; NE, $r = 0.47 \pm 0.06$; Extended Data Fig. 2d,h) and coherence (below 0.5 Hz; Extended Data Fig. 2e,i). This collinearity between ACh and Ca^{2+} was apparent when visually inspecting the respective time courses (Extended Data Fig. 2f) or plotting ACh against Ca^{2+} (Extended Data Fig. 2g, left). The same type of analysis revealed only a weak dependence between NE and Ca^{2+} (Extended Data Fig. 2g, right). Therefore, we decided to explore NE as a potential missing link affecting the relationship between the observed spontaneous Ca^{2+} signals and hemodynamics.

Accounting for NE dramatically improves hemodynamic estimation

First, we explored a linear regression model where the HbT time course was predicted, pixel by pixel, by a weighted sum of low-pass-filtered (<0.5 Hz) Ca^{2+} and global NE time courses (Fig. 2a). Assuming the causal neurovascular relationship, where the hemodynamic response follows neuronal activity, we allowed for a fixed delay between the neuronal variables and HbT estimated using an optimization algorithm for Ca^{2+} and NE (Fig. 2c and Methods). We further reasoned that the contribution of Ca^{2+} and NE to HbT fluctuations can vary in space. Although NE dynamics were very similar across our field of view (FOV) (Extended Data Fig. 2k), which is consistent with the literature[22], postsynaptic mechanisms, including the receptor type and density[23], can vary in space. Therefore, we introduced regression weights *A* (for Ca^{2+}) and *B* (for NE) for each pixel, each of which can be viewed as a map (Fig. 2b and Methods). With this model, *A* weights were consistently positive, indicating an increase in HbT (that is, vasodilation). Conversely, *B* weights were consistently negative, indicating a decrease in HbT (that is, vasoconstriction) (Fig. 2b and Extended Data Fig. 1f,g).

Compared to the IRF models with respect to Ca^{2+} alone (Ca^{2+}-IRF models; Fig. 1c–e), incorporation of NE dramatically improved the accuracy increasing the mean correlation (for all pixels) between the predicted and experimentally obtained HbT from 0.32 ± 0.02 ($n = 16$ subjects) to 0.60 ± 0.03 ($n = 8$ subjects; Fig. 2d,e and Extended Data Fig. 1d). Notably, the regression weights for the Ca^{2+} signal were high in cortical areas where performance of the global IRF was fair and low in those regions where Ca^{2+}-IRF models performed poorly (Fig. 1c,d versus Fig. 2b, left). The regression weights for the NE signal were typically more negative in regions where performance of Ca^{2+}-IRF models was poor (Fig. 1c,d versus Fig. 2b, right). Similar results were obtained when HbT was substituted by HbO or HbR (HbO, $r = 0.69 \pm 0.02$; HbR, $r = 0.67 \pm 0.01$; Extended Data Fig. 3).

Conceptually, these results suggest two parallel forces governing HbT behavior that are captured by Ca^{2+} (dilation) and NE (constriction) signals; the NE signal has a negative correlation with hemodynamic fluctuations and vessel diameter fluctuations observed in two-photon experiments (Extended Data Fig. 4). The influence of each of these forces on HbT varies across space. Therefore, we decided to explore whether the accuracy of the IRF model can be improved by incorporating two stationary IRFs (IRF_{Ca2+} and IRF_{NE}) along with space-varying weights *A* and *B* reflecting that contribution of Ca^{2+} and NE to HbT can vary in space. To devise this double IRF model, we used deconvolution to estimate IRF_{Ca2+} and IRF_{NE} from the data (Methods). The obtained IRF_{Ca2+} was consistently positive (that is, vasodilation), while IRF_{NE} was consistently negative (that is, vasoconstriction).

Similarly to the linear regression model, the double IRF model dramatically improved the prediction accuracy over Ca^{2+}-IRF models from 0.32 ± 0.02 ($n = 16$ subjects) to 0.59 ± 0.03 ($n = 8$ subjects) (Fig. 2a,f–i and Extended Data Fig. 1e) with high Ca^{2+} weights where Ca^{2+}-IRF models performed well and more negative NE weights where Ca^{2+}-IRF models performed poorly (Fig. 1c,d versus Fig. 2f). Similar results were obtained when HbT was substituted by HbO and HbR (HbO, $r = 0.67 \pm 0.03$; HbR, $r = 0.65 \pm 0.02$; Extended Data Fig. 3).

Because the spectral power of HbT declines rapidly above ~0.5 Hz (reflecting the slow nature of hemodynamics; Extended Data Fig. 2a), HbT signals in Fig. 2 were low-pass-filtered below 0.5 Hz to reject measurement noise (Methods). The use of unfiltered HbT, however, produced similar results (Extended Data Fig. 5). To validate the temporal dependence of HbT on NE, we shuffled NE data using a circular shift (25%, 50% and 75%) for each imaging session (Methods) and then fitted the linear regression and double IRF models using the shuffled data. As expected, NE shuffling reverted the model performance to that of the IRF models based on Ca^{2+} alone (Fig. 2j,k and Extended Data Fig. 5). As another control, we blocked NE receptors using a cocktail of α-adrenergic and β-adrenergic receptor blockers delivered intraperitoneally (Methods). In the presence of blockers, the IRF estimated pixel by pixel with respect to Ca^{2+} (the variant IRF model) had no undershoot, consistent with vasoconstrictive properties of NE,

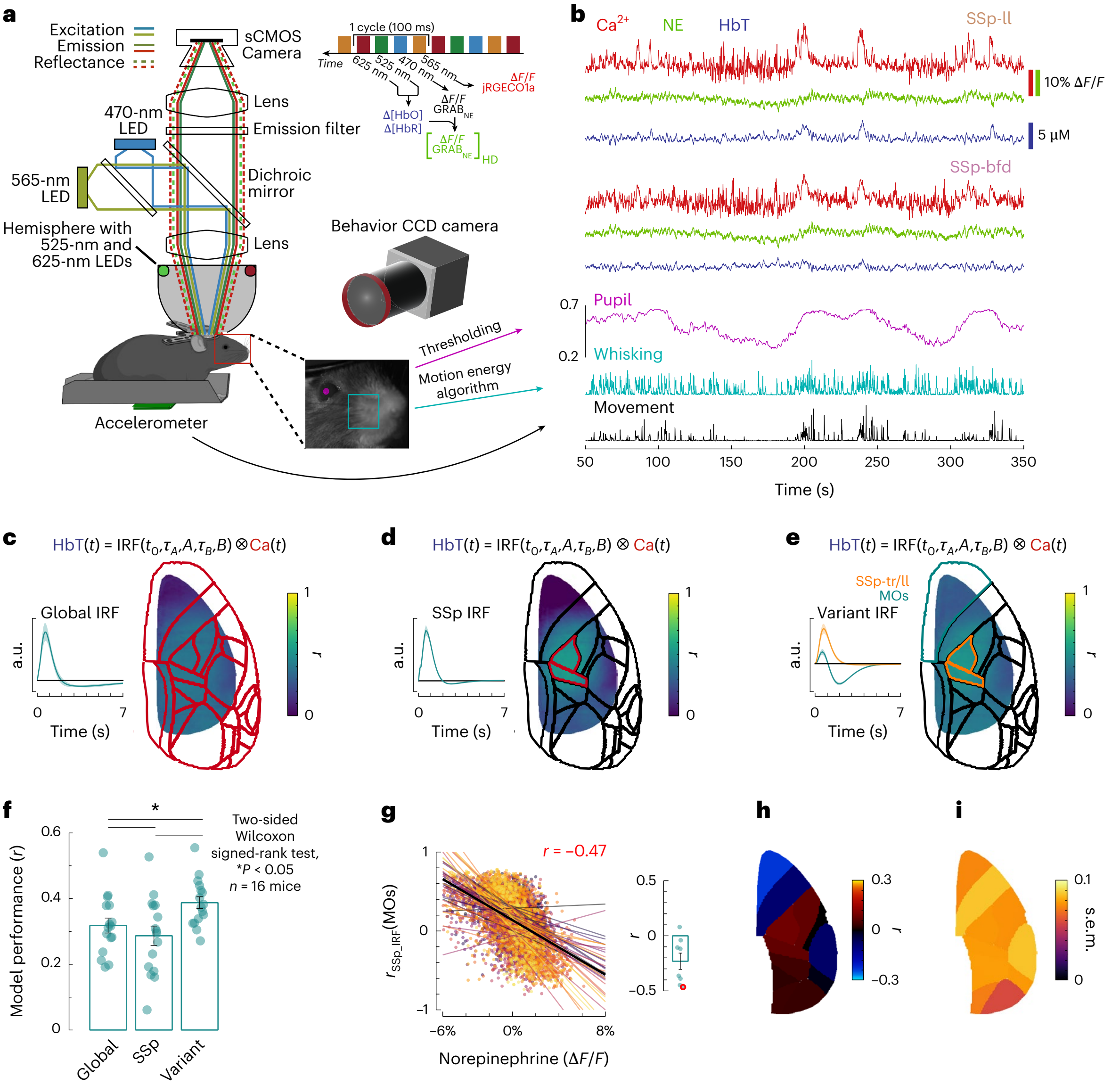

Fig. 1 | IRF linking spontaneous hemodynamics to neuronal Ca^{2+} varies across cortical space and time. a, Schematics of the mesoscopic imaging setup. Top right: timing of frame acquisition by the CMOS camera. Bottom right: an image of mouse face acquired by the CCD camera for quantification of the eye pupil and whisking. **b**, Example Ca^{2+}, NE and HbT time courses derived from two cortical regions, SSp-ll (top) and SSp-bfd (middle)[23], along with behavior readouts—the eye pupil, whisking and movement (bottom). **c**, Global IRF model. Left: estimated IRF from Ca^{2+} to HbT (mean ± s.e.m.). Right: model performance quantified as the correlation between the experimental and predicted HbT. First, for each subject, the correlation coefficient *r* was averaged pixel by pixel across runs. Then, 16 subjects were coregistered to the Allen Mouse Brain Atlas[23] and *r* was averaged pixel by pixel across subjects. **d**, Same as **c**, but using only the SSp-tr and SSp-ll regions for estimation of the IRF. **e**, Variant IRF model. Left: region-specific IRF for SSp-tr/ll (orange) and MOs (cyan). For each region, the IRF is an average of pixelwise IRFs for all pixels within that region (mean ± s.e.m.). Right: model performance (evaluated as in **c**; $n = 16$ subjects). **f**, Model performance across the models shown in **c**–**e**. For each subject and model, *r* was averaged across space. Each point represents one subject ($n = 16$ subjects; mean ± s.e.m.; $^{*}P < 0.05$, according to a paired, two-sided Wilcoxon signed-rank test; $r = 0.32 \pm 0.02$, 0.29 ± 0.03 and 0.39 ± 0.02 for the global, SSp and variant models, respectively). **g**, Accuracy of HbT prediction as a function of NE; pixelwise *r* was estimated using the SSp IRF model, averaged for all pixels within the MOs region and then plotted against the space-averaged (global) NE. Each point in the scatter plot corresponds to a 15-s sliding window within a 10-min run. A total of 36 runs acquired in one subject are overlaid. To facilitate visual inspection, for each run, we computed a slope; the average slope is shown in thick black. The *r* value (−0.47) was computed between the time course of the model performance in MOs and global NE for each run and then averaged across runs. Right: bar plot showing statistics across eight subjects for the same region ($n = 8$ subjects; mean ± s.e.m.; $r = -0.23 \pm 0.07$). **h**, The *r* value computed as in **g** for each cortical region averaged across eight subjects. **i**, Standard error of **h**.

and slow kinetics, possibly because of the role of NE in vascular tone[24] (Extended Data Fig. 6).

These results demonstrate that spontaneous hemodynamic fluctuations can be captured by a simple linear model with effective parameters describing the (dynamics of) dilatory and constrictive forces while also accounting for their varying influence across space.

Hemodynamic FC is a poor predictor of neuronal FC during arousal

The spatial specificity of the NE effect on hemodynamics implies that, for some cortical regions, reduction in hemodynamic coherence during arousal can occur despite coherent behavior of the underlying neuronal circuits. Indeed, close inspection of our data revealed instances of

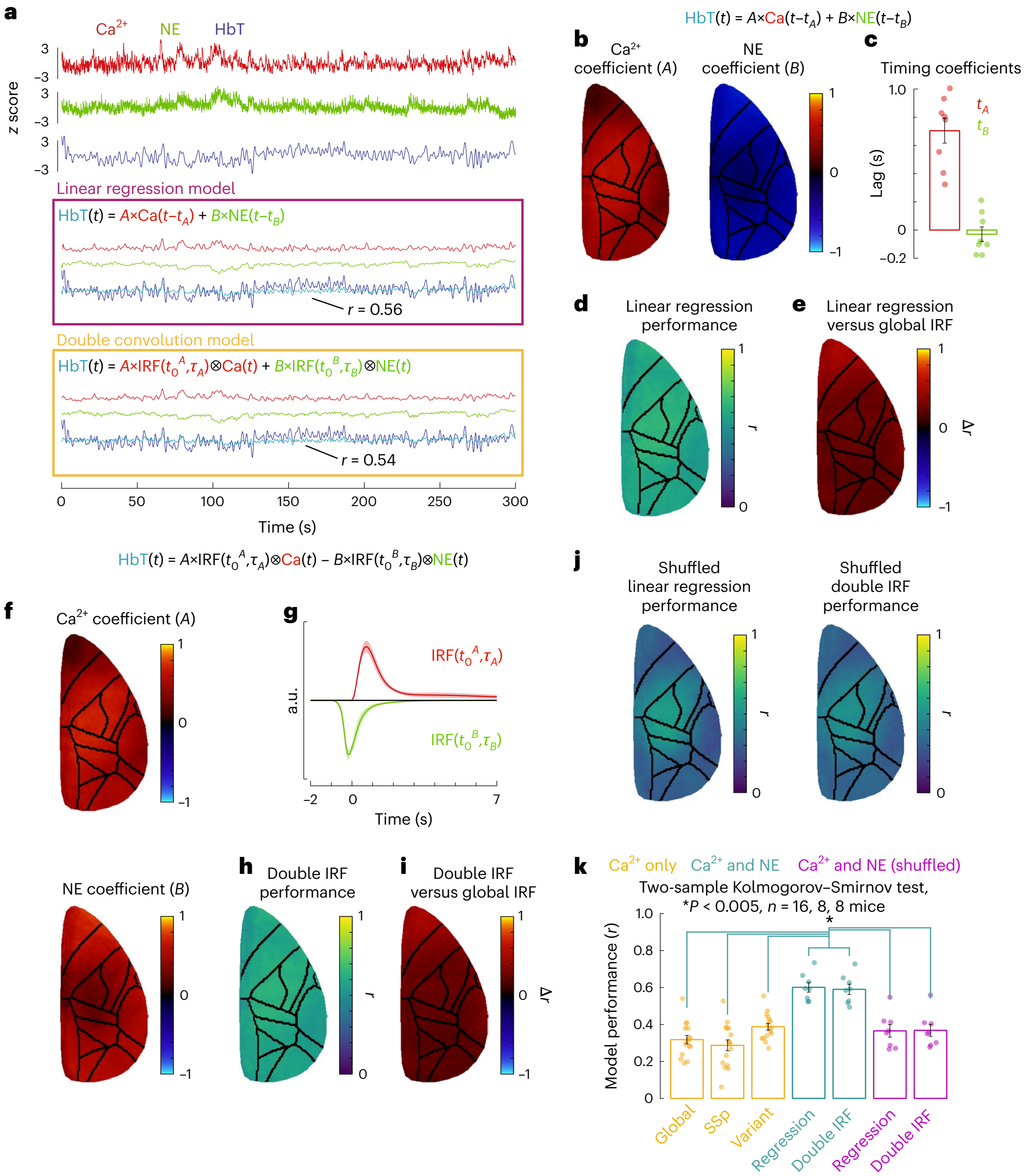

Fig. 2 | Spontaneous hemodynamic fluctuations depend on both Ca^{2+} and NE dynamics. a, Top: example Ca^{2+}, NE and HbT time courses derived from VISp cortical region expressed as *z* score. Middle: linear regression model showing time courses of Ca^{2+} and NE multiplied by their respective weights and shifted by their respective delays, with a comparison between experimental and predicted HbT (dark and light blue, respectively; $r = 0.56$). Bottom: double IRF model showing Ca^{2+} and NE convolution products multiplied by their respective weights, with a comparison between experimental and predicted HbT (dark and light blue, respectively; $r = 0.54$). **b**, Maps of the weights, *A* (left) and *B* (right), in the linear regression model ($n = 8$ subjects). **c**, Timing coefficients for Ca^{2+} and NE (t_A, t_B) for each subject ($n = 8$ subjects; mean ± s.e.m.; $t_A = 0.70 \pm 0.09$, $t_B = -0.03 \pm 0.05$). **d**, Linear regression model performance quantified as the correlation between the experimental and predicted HbT averaged across subjects ($n = 8$ subjects). **e**, Difference between linear regression model performance ($n = 8$ subjects) and global IRF model performance ($n = 16$ subjects). **f**,**h**,**i**, Same as **b**,**d**,**e**, but for the double IRF model ($n = 8$ subjects). **g**, Estimated IRF_{Ca2+} (red) and IRF_{NE} (green; $n = 8$ subjects; mean ± s.e.m.). **j**, Performance of the linear regression and double IRF models with reshuffled NE data ($n = 8$ subjects). **k**, Side-by-side model comparison. For each subject and model, the model performance (*r*) was averaged across space. Each point represents one subject ($*P < 0.005$, according to a two-sample, two-sided Kolmogorov–Smirnov test; mean ± s.e.m.; $r = 0.32 \pm 0.02$, 0.29 ± 0.03, 0.39 ± 0.02, 0.60 ± 0.03, 0.59 ± 0.03, 0.37 ± 0.03 and 0.37 ± 0.03 for the global, SSp, variant, linear regression, double IRF, linear regression with reshuffled NE and double IRF with reshuffled NE models, respectively; $n = 16$ subjects for the global, SSp, and variant models and $n = 8$ subjects for the double IRF and linear regression models).

divergent hemodynamic activity for pairs of cortical regions during high arousal (high NE and large eye pupil diameter) in the presence of coherent Ca^{2+} activity. Figure 3a–f illustrates this behavior for a specific pair of cortical regions, MOs and SSp-ll. Using cortical region-specific time courses for Ca^{2+} and HbT (Fig. 3a) and a 30-s sliding window, we obtained time courses of Ca^{2+} and hemodynamic FC (FC_{Ca2+} and FC_{HbT}, respectively; Fig. 3b and Methods). As a measure of similarity, we computed the correlation between the FC_{Ca2+} and FC_{HbT} matrices for each time window (r(FC_{Ca2+}, FC_{HbT}), Fig. 3c). Given the high similarity of NE signals across cortical space (Extended Data Fig. 2k), we plotted FC_{Ca2+} and FC_{HbT}, computed for each 30-s time window, as a function of global (that is, space-averaged) NE. This analysis revealed that FC_{Ca2+} consistently increased with an increase in NE, whereas FC_{HbT} was more variable but decreased on average (Fig. 3d). Thus, the correlation between FC_{Ca2+} and FC_{HbT} matrices decreased upon an increase in NE (Fig. 3e); this behavior was consistent across subjects (Fig. 3f).

To quantify the effect of NE across space, we used the Allen atlas[23] to define 12 primary cortical regions within the exposure and computed FC matrices during low and high NE (<30th percentile and >70th percentile, respectively; Methods), as well as the difference between the two (Fig. 3g,h). An increase in NE was associated with an increase in FC_{Ca2+} across all regions. FC_{HbT}, on the other hand, increased between some cortical regions (for example, MOs and VISp) but decreased between others (for example, MOs and SSp-II) (Fig. 3i,j). Spectral analysis revealed that the brain-region-specific effect of NE on FC_{HbT} was driven by low-frequency HbT (<0.1 Hz, peaking around 0.02 Hz) commonly used in resting-state studies (Extended Data Figs. 7 and 8).

The results in Fig. 3g–j are consistent with Fig. 2 showing high NE and low Ca^{2+} weights for the double IRF model in MOs and VISp (that is, dominant negative IRF_{NE}) and the opposite—high Ca^{2+} and low NE weights—in SSp-II (that is, dominant positive IRF_{Ca2+}). Indeed, regression of NE from HbT, pixel by pixel using the weighting coefficients from the linear regression model, removed localized negative correlations between the Ca^{2+} and HbT connectivity matrices (Extended Data Fig. 9).

Thus, vasoconstriction upon an increase in arousal and NE alters neurovascular coupling (NVC) with respect to neuronal Ca^{2+} in a region-specific way, resulting in a decrease in hemodynamic coherence between cortical regions with high and low NE weights. On the other hand, the correlation of Ca^{2+} activity between cortical regions generally increases upon an increase in the arousal/NE.

Discussion

Taken together, our results show that hemodynamic fluctuations accompanying spontaneous neuronal activity strongly depended on NE neuromodulation. While NVC with respect to neuronal Ca^{2+} was a dynamic and seemingly complex phenomenon, modeling the hemodynamic signal as a weighted sum of either (1) Ca^{2+} and NE time courses with the linear regression model or (2) stationary IRF_{Ca2+} and IRF_{NE} convolved with the respective Ca^{2+} and NE time courses with the double IRF model produced a high-accuracy fit to the data (0.60 ± 0.03 and 0.59 ± 0.03 accuracy, respectively). While this behavior was common for HbT, HbO and HbR, we hereafter discuss our results with respect to HbT as it is more directly related to arteriolar diameter, the physiological parameter directly controlled by vasoactive messenger molecules. Prior work on vascular responses evoked by sensory and OG stimulation by us and others demonstrated that dilatory and constrictive forces coexist and often result in a biphasic behavior of cortical arterioles[25–28]. In the current study, these forces were captured by the Ca^{2+} (dilation) and NE (constriction) coefficients, in both the linear regression and the double IRF models. The high accuracy of HbT prediction with these models suggests that feedforward, neurogenic regulation of CBF, which governs stimulus-induced hemodynamic responses[26,29–31], also applies to spontaneous (resting-state) neuronal activity. Therefore, analysis of resting-state and single-trial hemodynamic data should consider fluctuations in the arousal affecting NVC and IRF, as a failure to account for these effects may result in erroneous interpretations of hemodynamic coherence or lack thereof in terms of the underlying neuronal activity for some cortical regions.

Like other vasoactive neuromodulatory neurotransmitters, NE affects NVC in two ways: directly, by acting through adrenergic receptors on the vascular smooth muscle cells, and indirectly, by modulating the activity of local neuronal circuits and the associated release of vasoactive messengers[4]. Earlier studies that used electrical, OG or pharmacological stimulation of LC produced controversial results regarding dilation and constriction effects in the cerebral cortex[32,33]. This is in contrast with tissues outside the brain where activation of vascular adrenergic receptors consistently produces vasoconstriction[34]. Because NE often increases neuronal excitability[35–37], release of vasodilators from activated local cortical neurons can mask the vasoconstriction induced by the activation of vascular adrenergic receptors. In contrast to these perturbation approaches, we used a fluorescent biosensor $GRAB_{NE}$[14] to observe the release of NE in the context of naturally occurring brain activity. Under these conditions, NE was clearly correlated with a decrease in HbT in mesoscopic imaging and vasoconstriction in two-photon arteriolar diameter measurements. This finding is well aligned with a recent demonstration of a causal role of NE in driving cerebral vasoconstriction in mice[38] and zebrafish[39]. In our model, the direct vasoconstrictive effect of NE was reflected by IRF_{NE}, while its indirect effect was effectively included in IRF_{Ca2+}.

Prior stimulus-induced and resting-state hemodynamic studies that empirically characterized the IRF with respect to neuronal Ca^{2+} reported a range of IRF shapes and kinetics[21,31,40–44]. Multiple factors could contribute to these differences including the brain region, anesthetized versus awake conditions and the stimulus type. Furthermore, the same compound might exert distinct effects across cortical and subcortical brain regions depending on multiple factors including the receptor target[45]. While our model may generalize across the cerebral cortex (under awake resting-state conditions), it is less likely to perform well in subcortical regions that have specialized neuronal circuits and vasoactive compounds (for example, opioid signaling in the striatum[28]).

Mesoscale NE signals had low spatial granularity, which is in agreement with previous reports on the diffuse nature of NE projections in cerebral cortex[22]. Thus, the differences in NE weighting coefficients could be attributed to postsynaptic mechanisms including the type and density of (neuronal, astrocytic and vascular) adrenergic receptors and the density of target cortical neurons, for example, inhibitory interneurons expressing a vasoconstrictor neuropeptide Y (NPY)[46]. Because we captured most of the HbT variance (in the dorsal cerebral cortex) with a simple model that assumed a single constrictive force approximated with NE, it is tempting to speculate that other vasoconstrictors, such as NPY, exhibited collinearity with NE. The type of vasoactive compounds that dominate the control of (dilation and) constriction and their collinearity may depend on the brain state (for example, quiet rest versus goal-oriented behavior). If so, extending the current approach beyond the resting-state paradigm may generate a library of brain-state-dependent NVC models.

In contrast to NE, mesoscale ACh signals had high similarity to mesoscale Ca^{2+} signals filtered below ~0.5 Hz and, therefore, did not offer additive value to signals of Ca^{2+} alone for prediction of HbT. Modeling of light propagation in cortical tissue by us and others revealed that wide-field fluorescence imaging is mostly sensitive to signals within the top ~100 mm of cerebral cortex[47] (for example, cortical layer I that houses pyramidal apical dendritic tufts possessing voltage-gated Ca^{2+} channels[48]). Because activation of pyramidal neurons elicits vasodilation[26,49,50] and ACh is also a vasodilator[51], their respective vasodilatory effects would be lumped into the Ca^{2+} weighting coefficient in our linear regression and double IRF models. In the current study, we made no attempt to untangle these effects. In addition, we did not distinguish between ACh released by BF projections and that released by local cortical choline acetyltransferase vasoactive intestinal peptide interneurons[52]. Given the presence of local cholinergic axons in cortical layer I[53], high sensitivity of wide-field imaging to the cortical surface[47] and our recent findings of retinotopic ACh responses in the primary visual cortex[54], we believe that both sources contributed to the observed $GRAB_{ACh3.0}$ fluorescence.

In human BOLD fMRI studies, the eye pupil dilation was shown to correlate with deactivation of the default mode network (DMN)[55–57]. In

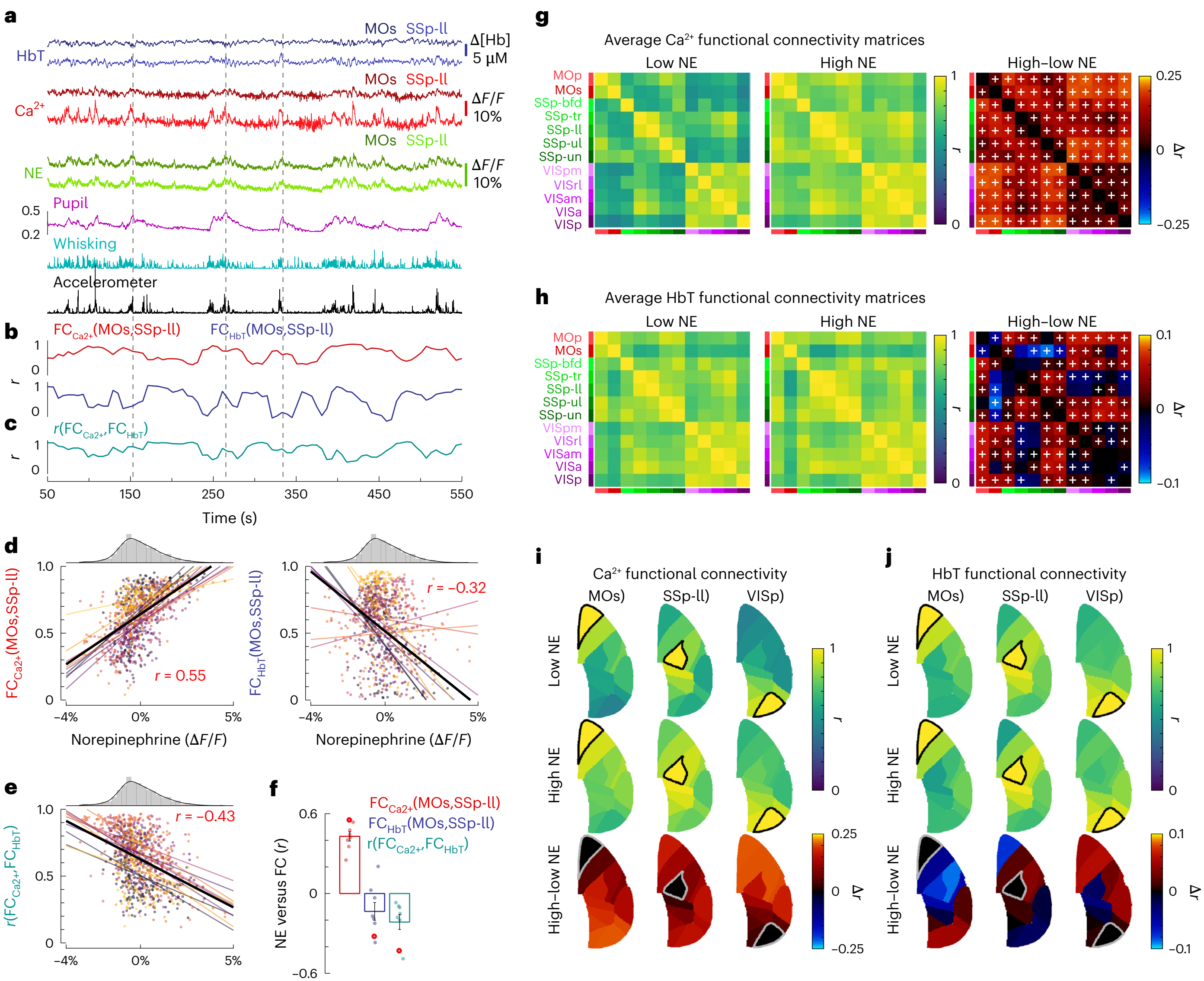

Fig. 3 | FC patterns between HbT and Ca^{2+} diverge during high arousal. **a**, Example Ca^{2+}, NE and HbT time courses derived from two cortical regions, MOs and SSp-ll, along with behavior readouts. The dashed vertical lines indicate NE peaks to facilitate visual inspection. **b**, Dynamic FC between MOs and SSp-ll for Ca^{2+} (red) and HbT (blue) computed as the correlation between the respective time courses using a 30-s sliding window. **c**, Correlation between Ca^{2+} and HbT connectivity matrices for each time window calculated using a 30-s sliding window. **d**, Dynamic FC between MOs and SSp-ll for Ca^{2+} (left) and HbT (right) as a function of NE. Each point on the scatter plot corresponds to a correlation coefficient for a 30-s sliding window plotted against global NE (averaged across space) within the same time window, with the NE values histogram shown above. Ten runs for one subject are overlaid. To facilitate visual inspection, for each run, we computed a slope; the average slope is shown in thick black. The *r* values (0.55 for Ca^{2+} and −0.32 for HbT) were computed between the dynamic FC time course and global NE for each run and then averaged across runs. **e**, Same as **d**, but plotting the correlation between Ca^{2+} and HbT connectivity matrices against NE using a 30-s sliding time window. The *r* value (−0.43) was computed similarly to **d**. **f**, Statistics across subjects. Red, correlation of dynamic FC and Ca^{2+} time courses from MOs and SSp-ll with global NE. Blue, correlation of dynamic FC and HbT time courses from MOs and SSp-ll with global NE. Cyan, correlation of Ca^{2+} and HbT connectivity matrices with global NE. Each point corresponds to one subject (average across runs). Data points for the subject shown in **d**,**e** are highlighted in red ($n = 8$ subjects; mean ± s.e.m.; $r = 0.43 \pm 0.03$, -0.13 ± 0.07 and -0.21 ± 0.06 for red, blue and cyan, respectively). **g**, Average Ca^{2+} connectivity matrices comparing connectivity during low NE (<30th percentile; left) and high NE (<70th percentile; middle). Right: difference between the high and low NE ($^{+}P < 0.05$, according to a two-sided linear mixed-effects model; comparisons between low and high NE were performed separately for each region pair; $n = 123$ sessions with eight subjects). **h**, Same as **g**, but for HbT ($n = 123$ sessions with eight subjects). **i**, Seed correlation maps comparing Ca^{2+} connectivity during low and high NE for MOs, SSp-ll and VISp regions ($n = 8$ subjects). **j**, Same as **i**, but for HbT ($n = 8$ subjects).

our data, the anterior cortical region where NE and eye pupil diameter were correlated with a decrease in HbT may belong, at least in part, to the mouse DMN analog[58–61]. Although firing rate decreases have been reported in other parts of DMN during (hemodynamic) deactivation[62], the present results suggest that active (signaling-driven) vasoconstriction should also be considered. A similar conclusion was reached in a recent mouse study that examined the effect of tonic chemogenetic activation of LC on the frontal cortex part of DMN[8].

The spatiotemporal patterns of FC in resting-state BOLD fMRI studies have become the principal means to investigate the integrity of large-scale functional networks in the human brain in health and disease[63]. Furthermore, the concept of dynamic FC was introduced in humans[64] and validated in animals[65,66]. The main underlying assumption in FC studies is that coherence of hemodynamic signals reflects synchronization of the underlying neuronal dynamics. Consistent with published studies, NE in our data was correlated with arousal: an increase in eye pupil diameter, whisking and body movement[2]. During high arousal, we observed instances of diminished hemodynamic coherence between cortical regions where HbT was differentially impacted by NE (for example, anterior versus medial somatosensory cortex) despite an increase in coherence of the underlying neuronal Ca^{2+} activity reflecting the functional integration role of NE[7,67]. Thus, the spatial specificity of NE affecting hemodynamics can lead to false interpretation of diminished FC as the underlying neuronal desynchronization during high arousal. Fortunately, high correlation of NE with the eye pupil diameter[21] may allow use of the eye pupil diameter as a surrogate for NE in fMRI studies where this measurement is readily attainable[55,57,68,69].

In contrast to a human resting-state fMRI study where subjects are typically instructed not to move, head-fixed mice exhibit intermittent whisking and body movements[70]. Furthermore, NE and the eye pupil diameter were highly correlated and fluctuations in the pupil diameter were typically associated with whisking and movement events. In other words, higher arousal was often associated with motor behavior. Although we could not dissociate arousal from movement, our data clearly demonstrate that NVC depends on the state of arousal and cortical region.

In our study, we used Ca^{2+} as a measure of the activity of local neuronal circuits. This measure is not available in humans. In humans, BOLD fMRI can be combined with electroencephalography (EEG), which offers a noninvasive measure of the extracellular electrical potential and has its own advantages, limitations and measurement theory[71]. Therefore, translation of the current results and take-home messages to humans requires tackling the relationship between the mesoscopic Ca^{2+} signals, which were used here, and surface electrical potentials that can be used for feedforward calculation of the corresponding EEG[29]; this is an ongoing effort in our collaboratory.

In this study, we demonstrate that spontaneous hemodynamic fluctuations can be captured by introducing effective parameters reflecting the underlying dilatory and constrictive forces. In reality, multiple signaling pathways contribute to each of these forces. Future studies will parse those pathways to offer the cell type and molecular specificity in the context of brain state and behavior. The most immediate implication of our present study for human resting-state fMRI is that diminished FC upon arousal may reflect the spatial specificity of the effect of neuromodulation on IRF rather than desynchronization of local cortical circuits.

Online content

Any methods, additional references, Nature Portfolio reporting summaries, source data, extended data, supplementary information, acknowledgements, peer review information; details of author contributions and competing interests; and statements of data and code availability are available at https://doi.org/10.1038/s41593-026-02239-7.

References

1. Chen, N., Sugihara, H. & Sur, M. An acetylcholine-activated microcircuit drives temporal dynamics of cortical activity. *Nat. Neurosci.* **18**, 892–902 (2015).
2. Breton-Provencher, V. & Sur, M. Active control of arousal by a locus coeruleus GABAergic circuit. *Nat. Neurosci.* **22**, 218–228 (2019).
3. Thiele, A. & Bellgrove, M. A. Neuromodulation of attention. *Neuron* **97**, 769–785 (2018).
4. Hamel, E. Perivascular nerves and the regulation of cerebrovascular tone. *J. Appl. Physiol. (1985)* **100**, 1059–1064 (2006).
5. Renden, R. B. et al. Modulatory effects of noradrenergic and serotonergic signaling pathway on neurovascular coupling. *Commun. Biol.* **7**, 287 (2024).
6. Biswal, B. et al. Functional connectivity in the motor cortex of resting human brain using echo-planar MRI. *Magn. Reson. Med.* **34**, 537–541 (1995).
7. Grimm, C. et al. Tonic and burst-like locus coeruleus stimulation distinctly shift network activity across the cortical hierarchy. *Nat. Neurosci.* **27**, 2167–2177 (2024).
8. Oyarzabal, E. A. et al. Chemogenetic stimulation of tonic locus coeruleus activity strengthens the default mode network. *Sci. Adv.* **8**, eabm9898 (2022).
9. Zerbi, V. et al. Rapid reconfiguration of the functional connectome after chemogenetic locus coeruleus activation. *Neuron* **103**, 702–718 (2019).
10. Pais-Roldan, P. et al. Contribution of animal models toward understanding resting state functional connectivity. *Neuroimage* **245**, 118630 (2021).
11. Turchi, J. et al. The basal forebrain regulates global resting-state fMRI fluctuations. *Neuron* **97**, 940–952 (2018).
12. Leopold, D. A. & Maier, A. Ongoing physiological processes in the cerebral cortex. *Neuroimage* **62**, 2190–2200 (2012).
13. Zaldivar, D. et al. Two distinct profiles of fMRI and neurophysiological activity elicited by acetylcholine in visual cortex. *Proc. Natl Acad. Sci. USA* **115**, E12073–E12082 (2018).
14. Feng, J. et al. Monitoring norepinephrine release in vivo using next-generation $GRAB_{NE}$ sensors. *Neuron* **112**, 1930–1942 (2024).
15. Jing, M. et al. A genetically encoded fluorescent acetylcholine indicator for in vitro and in vivo studies. *Nat. Biotechnol.* **36**, 726–737 (2018).
16. Jing, M. et al. An optimized acetylcholine sensor for monitoring in vivo cholinergic activity. *Nat. Methods* **17**, 1139–1146 (2020).
17. Sabatini, B. L. & Tian, L. Imaging neurotransmitter and neuromodulator dynamics in vivo with genetically encoded indicators. *Neuron* **108**, 17–32 (2020).
18. Doran, P. R. et al. Widefield in vivo imaging system with two fluorescence and two reflectance channels, a single sCMOS detector, and shielded illumination. *Neurophotonics* **11**, 034310 (2024).
19. Shahsavarani, S. et al. Cortex-wide neural dynamics predict behavioral states and provide a neural basis for resting-state dynamic functional connectivity. *Cell Rep.* **42**, 112527 (2023).
20. Lohani, S. et al. Spatiotemporally heterogeneous coordination of cholinergic and neocortical activity. *Nat. Neurosci.* **25**, 1706–1713 (2022).
21. Reimer, J. et al. Pupil fluctuations track rapid changes in adrenergic and cholinergic activity in cortex. *Nat. Commun.* **7**, 13289 (2016).
22. Pickel, V. M., Segal, M. & Bloom, F. E. A radioautographic study of the efferent pathways of the nucleus locus coeruleus. *J. Comp. Neurol.* **155**, 15–42 (1974).
23. Wang, Q. et al. The Allen Mouse Brain Common Coordinate Framework: a 3D reference atlas. *Cell* **181**, 936–953 (2020).
24. Korte, N. et al. Noradrenaline released from locus coeruleus axons contracts cerebral capillary pericytes via α_2 adrenergic receptors. *J. Cereb. Blood Flow Metab.* **43**, 1142–1152 (2023).
25. Devor, A. et al. Suppressed neuronal activity and concurrent arteriolar vasoconstriction may explain negative blood oxygenation level-dependent signal. *J. Neurosci.* **27**, 4452–4459 (2007).
26. Uhlirova, H. et al. Cell type specificity of neurovascular coupling in cerebral cortex. *eLife* **5**, e14315 (2016).
27. Vo, T. T. et al. Parvalbumin interneuron activity drives fast inhibition-induced vasoconstriction followed by slow substance P-mediated vasodilation. *Proc. Natl Acad. Sci. USA* **120**, e2220777120 (2023).

28. Cerri, D. H. et al. Distinct neurochemical influences on fMRI response polarity in the striatum. *Nat. Commun.* **15**, 1916 (2024).
29. Uhlirova, H. et al. The roadmap for estimation of cell-type-specific neuronal activity from non-invasive measurements. *Philos. Trans. R. Soc. Lond. B Biol. Sci.* **371**, 20150356 (2016).
30. Cauli, B. & Hamel, E. Revisiting the role of neurons in neurovascular coupling. *Front. Neuroenergetics* **2**, 9 (2010).
31. Drew, P. J. Vascular and neural basis of the BOLD signal. *Curr. Opin. Neurobiol.* **58**, 61–69 (2019).
32. Toussay, X. et al. Locus coeruleus stimulation recruits a broad cortical neuronal network and increases cortical perfusion. *J. Neurosci.* **33**, 3390–3401 (2013).
33. Raichle, M. E. et al. Central noradrenergic regulation of cerebral blood flow and vascular permeability. *Proc. Natl Acad. Sci. USA* **72**, 3726–3730 (1975).
34. Segal, S. S., Damon, D. N. & Duling, B. R. Propagation of vasomotor responses coordinates arteriolar resistances. *Am. J. Physiol.* **256**, H832–H837 (1989).
35. O'Donnell, J. et al. Norepinephrine: a neuromodulator that boosts the function of multiple cell types to optimize CNS performance. *Neurochem. Res.* **37**, 2496–2512 (2012).
36. Labarrera, C. et al. Adrenergic modulation regulates the dendritic excitability of layer 5 pyramidal neurons in vivo. *Cell Rep.* **23**, 1034–1044 (2018).
37. Deitcher, Y. et al. Nonlinear relationship between multimodal adrenergic responses and local dendritic activity in primary sensory cortices. Preprint at *bioRxiv* https://doi.org/10.1101/814657 (2019).
38. Hauglund, N. L. et al. Norepinephrine-mediated slow vasomotion drives glymphatic clearance during sleep. *Cell* **188**, 606–622 (2025).
39. Sun, L. et al. Globally patterned locus coeruleus–norepinephrine neuron–pericyte coupling orchestrates brain-wide vascular dynamics. *Neuron* **114**, 287–306 (2026).
40. Chao, T. H. et al. Computing hemodynamic response functions from concurrent spectral fiber-photometry and fMRI data. *Neurophotonics* **9**, 032205 (2022).
41. Zhang, W. T. et al. Spectral fiber photometry derives hemoglobin concentration changes for accurate measurement of fluorescent sensor activity. *Cell Rep. Methods* **2**, 100243 (2022).
42. Ma, Z. et al. Gaining insight into the neural basis of resting-state fMRI signal. *Neuroimage* **250**, 118960 (2022).
43. Tong, C. et al. Differential coupling between subcortical calcium and BOLD signals during evoked and resting state through simultaneous calcium fiber photometry and fMRI. *Neuroimage* **200**, 405–413 (2019).
44. Drew, P. J. Neurovascular coupling: motive unknown. *Trends Neurosci.* **45**, 809–819 (2022).
45. Jenkins, B. G. Pharmacologic magnetic resonance imaging (phMRI): imaging drug action in the brain. *Neuroimage* **62**, 1072–1085 (2012).
46. Smialowska, M., Gastol-Lewinska, L. & Tokarski, K. The role of α-1 adrenergic receptors in the stimulating effect of neuropeptide Y (NPY) on rat behavioural activity. *Neuropeptides* **26**, 225–232 (1994).
47. Tian, P. et al. Monte Carlo simulation of the spatial resolution and depth sensitivity of two-dimensional optical imaging of the brain. *J. Biomed. Opt.* **16**, 016006 (2011).
48. Major, G., Larkum, M. E. & Schiller, J. Active properties of neocortical pyramidal neuron dendrites. *Annu. Rev. Neurosci.* **36**, 1–24 (2013).
49. Lacroix, A. et al. COX-2-derived prostaglandin E2 produced by pyramidal neurons contributes to neurovascular coupling in the rodent cerebral cortex. *J. Neurosci.* **35**, 11791–11810 (2015).
50. Lecrux, C. et al. Pyramidal neurons are 'neurogenic hubs' in the neurovascular coupling response to whisker stimulation. *J. Neurosci.* **31**, 9836–9847 (2011).
51. Nishimura, N. et al. Limitations of collateral flow after occlusion of a single cortical penetrating arteriole. *J. Cereb. Blood. Flow Metab.* **30**, 1914–1927 (2010).
52. Granger, A. J. et al. Cortical ChAT$^+$ neurons cotransmit acetylcholine and GABA in a target- and brain-region-specific manner. *eLife* **9**, e57749 (2020).
53. Obermayer, J. et al. Prefrontal cortical ChAT-VIP interneurons provide local excitation by cholinergic synaptic transmission and control attention. *Nat. Commun.* **10**, 5280 (2019).
54. Knudstrup, S. G. et al. Visual stimulation drives retinotopic acetylcholine release in the mouse visual cortex. Preprint at *bioRxiv* https://doi.org/10.1101/2024.02.04.578821 (2024).
55. Schneider, M. et al. Spontaneous pupil dilations during the resting state are associated with activation of the salience network. *Neuroimage* **139**, 189–201 (2016).
56. DiNuzzo, M. et al. Brain networks underlying eye's pupil dynamics. *Front. Neurosci.* **13**, 965 (2019).
57. Yellin, D., Berkovich-Ohana, A. & Malach, R. Coupling between pupil fluctuations and resting-state fMRI uncovers a slow build-up of antagonistic responses in the human cortex. *Neuroimage* **106**, 414–427 (2015).
58. Gozzi, A. & Schwarz, A. J. Large-scale functional connectivity networks in the rodent brain. *Neuroimage* **127**, 496–509 (2016).
59. Grandjean, J. et al. Common functional networks in the mouse brain revealed by multi-centre resting-state fMRI analysis. *Neuroimage* **205**, 116278 (2020).
60. Xu, N. et al. Functional connectivity of the brain across rodents and humans. *Front. Neurosci.* **16**, 816331 (2022).
61. Whitesell, J. D. et al. Regional, layer, and cell-type-specific connectivity of the mouse default mode network. *Neuron* **109**, 545–559 (2021).
62. Hayden, B. Y., Smith, D. V. & Platt, M. L. Electrophysiological correlates of default-mode processing in macaque posterior cingulate cortex. *Proc. Natl Acad. Sci. USA* **106**, 5948–5953 (2009).
63. van den Heuvel, M. P. & Sporns, O. A cross-disorder connectome landscape of brain dysconnectivity. *Nat. Rev. Neurosci.* **20**, 435–446 (2019).
64. Hutchison, R. M. et al. Dynamic functional connectivity: promise, issues, and interpretations. *Neuroimage* **80**, 360–378 (2013).
65. Benisty, H. et al. Rapid fluctuations in functional connectivity of cortical networks encode spontaneous behavior. *Nat. Neurosci.* **27**, 148–158 (2024).
66. Higley, M. J. & Cardin, J. A. Spatiotemporal dynamics in large-scale cortical networks. *Curr. Opin. Neurobiol.* **77**, 102627 (2022).
67. Shine, J. M. Neuromodulatory influences on integration and segregation in the brain. *Trends Cogn. Sci.* **23**, 572–583 (2019).
68. Pais-Roldán, P. et al. Indexing brain state-dependent pupil dynamics with simultaneous fMRI and optical fiber calcium recording. *Proc. Natl Acad. Sci. USA* **117**, 6875–6882 (2020).
69. Sobczak, F. et al. Decoding the brain state-dependent relationship between pupil dynamics and resting state fMRI signal fluctuation. *eLife* **10**, e68980 (2021).
70. Drew, P. J. et al. Ultra-slow oscillations in fMRI and resting-state connectivity: neuronal and vascular contributions and technical confounds. *Neuron* **107**, 782–804 (2020).
71. Halnes, G. et al., *Electric Brain Signals: Foundations and Applications of Biophysical Modeling* (Cambridge University Press, 2024).

---

[1]Graduate program in Biomedical Engineering, Boston University, Boston, MA, USA. [2]Department of Biomedical Engineering, Boston University, Boston, MA, USA. [3]Graduate program in Biology, Boston University, Boston, MA, USA. [4]Undergradute program in Neuroscience, Boston University, Boston, MA, USA. [5]Graduate Program for Neuroscience (GPN), Boston University, Boston, MA, USA. [6]Graduate Program in Pharmacology and Experimental Therapeutics, Boston University, Boston, MA, USA. [7]Department of Biology, Boston University, Boston, MA, USA. [8]Edmond and Lily Safra Center for Brain Sciences and Alexander Silberman Institute of Life Sciences, The Hebrew University of Jerusalem, Jerusalem, Israel. [9]Department of Physics, University of California, San Diego, La Jolla, CA, USA. [10]Department of Neurobiology, University of California, San Diego, La Jolla, CA, USA. [11]Department of Psychological & Brain Sciences, Boston University, Boston, MA, USA. [12]Athinoula A. Martinos Center for Biomedical Imaging, Department of Radiology, Harvard Medical School, Massachusetts General Hospital, Charlestown, MA, USA. [13]IMES and EECS, Massachusetts Institute of Technology, Cambridge, MA, USA. [14]Department of Electrical and Computer Engineering, Boston University, Boston, MA, USA. [15]Halıcıoğlu Data Science Institute and Department of Computer Science and Engineering, University of California, San Diego, La Jolla, CA, USA. [16]Department of Mathematics & Statistics, Boston University, Boston, MA, USA. [17]These authors contributed equally: Bradley C. Rauscher, Natalie Fomin-Thunemann. ✉e-mail: adevor@bu.edu

Methods

Experimental animals

All experimental procedures were performed in accordance with the guidelines established by the Boston University Institutional Animal Care and Use Committee. Standard rodent chow and water were provided ad libitum. Mice were housed in a 12-h light cycle with lights turning on at 7:30 a.m. We used 20 adult mice of either sex from the Thy1-jRGECO1a GP8.20 line[72]. Cortex-wide expression of $GRAB_{NE3.1}$ and $GRAB_{NE\text{-}mutant}$ was induced by retro-orbital virus injection of adeno-associated virus (AAV) with PHP.eB serotypes (BrainVTA, PT-1344, rAAV-hSyn-NE3.1,AAV2/PHP.eB or rAAV-hSyn-NE2m-mut, AAV2/PHP.eB; 2×10^{13} viral genomes per ml, 50 µl used) in adult mice (6–9 weeks old)[73]. Cortex-wide expression of $GRAB_{ACh3.0}$ was induced by either (1) virus injection of 1.5 µl of AAVs (for example, AAV9-hSyn-$GRAB_{ACh3.0}$ (WZ Biosciences or BrainVTA); 3.06×10^{13} genome copies per ml) into each transverse sinus (3 µl per animal) in 1-day-old neonates[20] or (2) retro-orbital virus injection of AAVs with PHP.eB serotypes as with $GRAB_{NE}$ in adult mice (6–9 weeks old)[73].

Animal procedures

The surgical procedure was modified from that previously described[74,75]. Dexamethasone was injected ~4 h before surgery (intraperitoneal 4.8 mg kg^{-1} at 4 mg ml^{-1} concentration) to prevent brain swelling because of surgical intervention. In addition, slow-release buprenorphine and meloxicam were injected before surgery. During surgery, mice were anesthetized with either isoflurane (2% in O_2 initially, 1% in O_2 during all procedures), ketamine/xylazine or a mixture of medetomidine, midazolam and fentanyl and their body temperature was maintained at 37 °C. A custom-designed headpost machined from titanium was attached to the cranium. Two pieces of curved or flat glass were used to replace the dorsal cranium, one per hemisphere[75]. To prevent heat loss through the window, either silicone or cotton was placed on top of the glass window and contained with a protective three-dimensionally printed cap fixed to the headpost. Mice were allowed to recover for at least 1 week following surgery before habituation to head fixation and at least 3 weeks before experiments.

Behavioral training and recording

Starting at least 1 week after the surgical procedure, mice were habituated in daily sessions to accept increasingly longer periods of head restraint (up to 2 h). During the head restraint, the animal was placed on a suspended bed. A drop of sweetened condensed milk was offered a few times during the fixation as a reward. Habituated head-fixed mice consumed the reward milk and often exhibited periods of putative sleep, defined as eye pupil constriction accompanied by a large-amplitude, prolonged vasodilation[76]. Mice were free to readjust their body position and, from time to time, displayed natural grooming behavior. In both mesoscopic and two-photon experiments, a charge-coupled device (CCD) camera (Basler, acA1920-150uc) with a variable-zoom lens (Edmund Optics, 67715) was used for continuous observation of the mouse face during imaging. In two-photon experiments, we used a 940-nm light-emitting diode (LED; Thorlabs, M940L3) to illuminate the face of the animal and a 920-nm long-pass filter to prevent illumination light from reaching photomultiplier tube (PMT) detectors. In one-photon experiments, we used a 940-nm LED (Thorlabs, M940L3) to illuminate the face of the animal. The camera frames were synchronized with image acquisition and recorded. In addition, an accelerometer (Analog Devices, ADXL335) was placed underneath the mouse bed to record the animal motion. Periods of putative sleep were excluded from data analysis.

Mesoscopic imaging

Wide-field imaging was performed using a home-built mesoscope described previously[18] (Fig. 1a). A single scientific complementary metal–oxide–semiconductor (CMOS) camera coupled to an objective lens (Olympus ZDM-1-MVX063) was used to sequentially record four channels: a green fluorescence channel for imaging of $GRAB_{NE}$ or $GRAB_{ACh}$, a red fluorescence channel for imaging of jRGECO1a and two reflectance channels at 525 nm and 625 nm for quantification of HbO/HbR/HbT. A 10 × 10-mm FOV covered the entire dorsal cortex. Images were acquired at 10 Hz, with a spatial resolution of 20 µm at 4 × 4 binning. Fluorescence excitation was achieved through epi-illumination. For GRAB excitation, a 470-nm LED (ThorLabs, SOLIS-470C) was used with a 466/40-nm bandpass filter (Semrock). For jRGECO1a excitation, a 565-nm LED (ThorLabs, SOLIS-565C) was used with a 560/14-nm bandpass filter (Semrock) and an additional 450-nm long-pass filter (Chroma) to eliminate a secondary emission peak around 425 nm. The emission pathway included a dual-band dichroic mirror (488/561 nm; Semrock) and a multiband filter (523/610 nm; Semrock). This configuration allowed GRAB and jRGECO1a fluorescence (500–540 nm and 580–640 nm, respectively) to reach the detector while blocking excitation light (440–480 nm and 550–570 nm). For imaging of reflectance, illumination LEDs were positioned in a ring around the objective and an aluminum hemisphere was placed between the objective and cranial window to provide diffuse illumination[18]. The estimated changes in HbO and HbR were used to correct fluorescence signals for the hemodynamic artifact[77].

Data were acquired in 10-min ‘runs’. Multiple runs were acquired on each experimental day for one mouse and each mouse was imaged on multiple days (Supplementary Table 1)

Two-photon imaging

Images were obtained using an Ultima two-photon laser scanning microscopy system (Bruker Fluorescence Microscopy). The GRAB sensor ($GRAB_{NE}$ or $GRAB_{ACh}$) and jRGECO1a were coexcited at 990 nm using a Discovery laser (Coherent) (Extended Data Fig. 4). Emitted light was filtered (GRAB: 525/50 nm; jRGECO1a: 617/73 nm) and directed to cooled GaAsP detectors (Hamamatsu, H7422P-40). For imaging of vasodilation, Alexa Fluor 680 was conjugated to amino-dextran (molecular weight = 2 MDa; Finabio, AD2000x100)[78] and injected intravenously (50–100 µl of 5% (w/v) solution in saline). Alexa Fluor 680 was excited using the same 990-nm beam and imaged using a multialkali PMT (R3896, Hamamatsu). In the absence of jRGECO1a, the GRAB sensor and Alexa Fluor 680 were coexcited at 950 nm.

We used a ×4 objective (Olympus XLFluor4x/340, numerical aperture (NA) = 0.28) to obtain low-resolution images of the exposure. The Olympus ×20 (XLUMPlanFLNXW, NA = 1.0) water-immersion objective was used for high-resolution imaging. Measurements were performed in a frame-scan mode at 5–10 Hz.

Vessel diameter was extracted from Alexa Fluor 680 images by defining an ROI surrounding the penetrating arteriole and counting the number of pixels above a preset intensity threshold. We then calculated the change in diameter relative to the average diameter over the 10-min run. To extract the Ca^{2+} and NE time courses from jRGECO1a and $GRAB_{NE}$ images, we averaged fluorescence within the FOV, excluding an ROI placed around the penetrating arteriole to avoid averaging the arteriole’s shadow.

Noradrenergic receptor blocker preparation and experiments

Prazosin hydrochloride was dissolved in DMSO to a concentration of 25 mM, propranolol was dissolved in water to a concentration of 20 mM and the pH was adjusted to 3 with HCl, atipamezole was obtained as a pharmaceutical-grade preparation with a concentration of 5 mg ml^{-1}. Stock solutions were prewarmed in a water bath to 37 °C. Stock solutions were diluted in prewarmed 0.9% NaCl for an injection volume of 500 µl with 10 mg kg^{-1} prazosin, 10 mg kg^{-1} propranolol and 1 mg kg^{-1} atipamezole. The solution was sonicated before administration through intraperitoneal injection.

Before injection, two baseline 10-min imaging sessions were recorded. Then, 30 min after injection, six 10-min imaging sessions, spanning 30 to 90 min after injection, were recorded.

Immunohistochemistry

Mice were killed and transcardially perfused with heparinized PBS followed by 4% paraformaldehyde (PFA). The brain was removed immediately after perfusion and postfixed in 4% PFA overnight at 4 °C. The brain was then washed three times with PBS and stored at 4 °C in a 30% sucrose solution for at least 3 days. Brain tissue was cut into 40-µm coronal or sagittal sections using a cryostat (Leica CM1950) and stored in Tris-buffered saline (TBS) containing 0.01% sodium azide at 4 °C. Tissue sections were processed for immunofluorescence staining using free-floating staining protocols as previously described[79]. In short, antigen retrieval was performed by incubating tissue sections in a 1 N hydrochloric acid solution for 10 min followed by three washes with TBS. Sections were blocked and permeabilized in TBS containing 5% donkey serum and 0.5% Triton X-100 for 1 h. The primary antibody solution was applied to tissue sections overnight at 4 °C and consisted of chicken anti-GFP (1:1,000; Abcam, ab13970) diluted in TBS buffer. Tissue sections were then incubated for 2 h in the secondary antibody solution consisting of Alexa Fluor 488 donkey anti-chicken (1:250; Jackson ImmunoResearch, AB_2340375), diluted in TBS containing 5% donkey serum. Cell nuclei were stained with DAPI (2 ng ml^{-1}; Molecular Probes) for 15 min. Tissue sections were mounted onto slides using ProLong gold antifade reagent (Invitrogen, P36934) and imaged in the epifluorescence mode on an IX83 Olympus microscope.

Hemodynamic correction

Mesoscopic data preprocessing and hemodynamic correction of the fluorescence channels were performed as described previously[18]. Briefly, the modified Beer–Lambert law was used to calculate changes in HbO and HbR concentrations from 525 nm and 625 nm reflectance. Estimated Δ[HbO] and Δ[HbR] were then used to correct the green (GRAB$_{\mathrm{NE}}$/GRAB$_{\mathrm{ACh3.0}}$) and red (jRGECO1a) channels[19,77]. We adjusted the scattering coefficient (μ_s) for the excitation path (470 nm) to 85.2 cm^{-1} and for the emission path (515 nm) to 70.9 cm^{-1} using data obtained in in C57BL/6 mice expressing the GRAB$_{\mathrm{NE\text{-}mutant}}$ sensor, which does not respond to NE. After preprocessing, mesoscopic images were smoothed in space using a Gaussian kernel with full width at half maximum of two pixels.

Behavior measurements

To calculate the eye pupil diameter, an elliptical region was drawn defining the eye and an intensity threshold was defined as the average of the intensity of the pupil and the surrounding iris. This pupil size was calculated as the number of pixels below this threshold and adjusted to represent pupil diameter in reference to the visible diameter of the eye, ranging from 0 to 1. To quantify whisking, a rectangular region was drawn over the whisker pad and a motion energy algorithm was used to estimate whisking behavior[80]. For the accelerometer recording, we first subtracted the mean, took the absolute value and downsampled to the acquisition frequency of optical imaging (10 Hz).

Alignment with the Allen Mouse Brain Atlas

Mesoscopic images were aligned to the Allen Mouse Brain Atlas[23] for region-specific analysis. First, a two-dimensional representation of the Allen atlas was rigidly aligned to a reference functional map for each mesoscopic imaging session (s.d. in time of jRGECO1a channel; Extended Data Fig. 10c). Next, 12 region masks were extracted (MOp, MOs, SSp-bfd, SSp-tr, SSp-ll, SSp-ul, SSp-un, VISpm, VISrl, VISam, VISa and VISp). These regions were chosen as they were always visible within the optical window. The masks were trimmed if needed along the window edge for each subject.

Global IRF and SSp IRF model

Before IRF estimation, HbT signals were low-pass-filtered below 0.5 Hz using a sixth-order Butterworth filter (MATLAB). Next, HbT and Ca^{2+} signals were normalized, pixelwise, to their s.d. in time to remove bias toward pixels with larger variance. With a global, stationary IRF model, HbT at time t is expressed as follows:

$$\mathrm{HbT}\,(t) = \mathrm{Ca}^{2+}\,(t) \circledast \mathrm{IRF}(t) \tag{1}$$

where ⊛ is the convolution operator. The IRF is invariant with respect to location within the exposure or time in the session. To ease computational burden for the optimization algorithm, 4 × 4 spatial binning was applied to the HbT and Ca^{2+} signals. To estimate the IRF, we deconvolved the HbT signal with the Ca^{2+} signal using the matrix formulation below, where T is the number of time points in the 10-min run (6,000 total time points given 10 Hz acquisition) and N is the number of pixels in our exposure.

$$\begin{bmatrix} \mathrm{Ca}_1^1 & 0 & 0 & \dots & 0 \\ \mathrm{Ca}_2^1 & \mathrm{Ca}_1^1 & 0 & \dots & 0 \\ \mathrm{Ca}_3^1 & \mathrm{Ca}_2^1 & \mathrm{Ca}_1^1 & \dots & 0 \\ \dots & \dots & \dots & \dots & \dots \\ \mathrm{Ca}_{T-1}^1 & \mathrm{Ca}_{T-2}^1 & \mathrm{Ca}_{T-3}^1 & \dots & \mathrm{Ca}_{T-100}^1 \\ \mathrm{Ca}_T^1 & \mathrm{Ca}_{T-1}^1 & \mathrm{Ca}_{T-2}^1 & \dots & \mathrm{Ca}_{T-99}^1 \\ \dots & \dots & \dots & \dots & \dots \\ \mathrm{Ca}_1^N & 0 & 0 & \dots & 0 \\ \dots & \dots & \dots & \dots & \dots \\ \mathrm{Ca}_T^N & \mathrm{Ca}_{T-1}^N & \mathrm{Ca}_{T-2}^N & \dots & \mathrm{Ca}_{T-99}^N \end{bmatrix} \times \begin{bmatrix} \mathrm{IRF}_1 \\ \mathrm{IRF}_2 \\ \mathrm{IRF}_3 \\ \dots \\ \mathrm{IRF}_{99} \\ \mathrm{IRF}_{100} \end{bmatrix} = \begin{bmatrix} \mathrm{HbT}_1^1 \\ \mathrm{HbT}_2^1 \\ \mathrm{HbT}_3^1 \\ \dots \\ \mathrm{HbT}_{T-1}^1 \\ \mathrm{HbT}_T^1 \\ \dots \\ \mathrm{HbT}_1^N \\ \dots \\ \mathrm{HbT}_T^N \end{bmatrix}$$

We assumed the following functional form of the IRF adopted from a previous study[25]:

$$\mathrm{IRF}(t) = A \times \left(\frac{t - t_0}{\tau_\mathrm{D}}\right)^3 \times e^{-\frac{t - t_0}{\tau_\mathrm{D}}} + B \times \left(\frac{t - t_0}{\tau_\mathrm{C}}\right)^3 \times e^{-\frac{t - t_0}{\tau_\mathrm{C}}} \tag{2}$$

where $t_0 \geq 0$, A and B are scalar coefficients and t_D and t_C are dilation and constriction time constants, respectively. We simultaneously fit for five parameters (t_0, A, B, t_D and t_C) in MATLAB (R2022a) using the ‘fmincon’ function to obtain a 10-s (100 time points given 10-Hz acquisition) IRF.

To evaluate the accuracy of this model across cortical space, we convolved, pixel by pixel, the estimated global IRF with the original (not spatially binned) Ca^{2+} signal to predict HbT. We then computed, pixel by pixel, the correlation between the predicted and experimentally obtained HbT using the entire duration of the data run (10 min). Overall model performance was defined as the average correlation coefficient within the standard FOV shown in Extended Data Fig. 1. The standard FOV was defined only for the right hemisphere. All imaging sessions were first aligned to the Allen Mouse Brain Atlas[23]. Using the Allen atlas regions as landmarks, runs were then registered to the standard FOV. For subjects where only the left hemisphere was available (for example, subject Thy1_296; Supplementary Table 1), the FOV was mirrored across the midline. To calculate the average model performance map, maps were first aligned to the standard FOV and averaged within each subject. The resulting average (and aligned) maps were then averaged across subjects.

To explore dependence of the model accuracy on neuromodulation dynamics, we used a 15-s sliding window to compute (1) the correlation between the estimated and experimentally obtained HbT and (2) the global NE signal (averaged across space). The latter was motivated by observing that NE was largely uniform across the cortex. Then, for each 15-s time window, we plotted the correlation between the estimated and experimentally obtained HbT as a function of the mean NE in a scatter plot (Supplementary Video 2).

The same algorithm was used for SSp IRF model except that we only considered pixels within the SSp-tr and SSp-ll cortical regions for estimation of the IRF kernel. This IRF kernel was then used to predict HbT across all pixels within the exposure.

Variant IRF model

Before IRF estimation, HbT signals were low-pass-filtered below 0.5 Hz using a sixth-order Butterworth filter (MATLAB). Next, HbT and Ca^{2+} signals were normalized, pixelwise, to their s.d. in time to remove bias toward pixels with larger variance. With a variant IRF model, HbT is expressed as in Eq. 1; however, the weights of the individual alpha functions (A and B in Eq. 2) are allowed to vary across pixels and the timing coefficient (t_0, t_C and t_D in Eq. 2) are kept constant across space. Because of added computational complexity, a 32 × 32 spatial binning factor was applied to the HbT and Ca^{2+} signals.

Again, we simultaneously fit for the three timing parameters and the N alpha function weights (A and B) in MATLAB (R2022a) using the 'fmincon' function to obtain a 10-s IRF kernel for each 32 × 32 pixel bin. To extend to the original (not spatially binned) signals, we convolved, pixel by pixel, the original Ca^{2+} signal with both individual alpha functions using the optimized timing parameters and weights (A and B) of Eq. 1. This resulted in two Ca^{2+} time courses associated with each of the alpha functions. We then used linear regression, pixel by pixel, using the backslash operator in MATLAB to estimate the spatially varying weights (A and B) across space.

To evaluate the accuracy of this model across cortical space, we convolved, pixel by pixel, the pixel-specific IRF kernel with the original (not spatially binned) Ca^{2+} signal to predict HbT. We then computed, pixel by pixel, the correlation between the predicted and experimentally obtained HbT using the entire duration of the data run (10 min).

Linear regression model

In our linear regression model, HbT is expressed as follows:

$$\begin{aligned}\mathrm{HbT}\,(t) &= A \times \mathrm{Ca}^{2+}\,(t - t_A) + B \times \mathrm{NE}(t - t_B)\\ &= A \times \mathrm{Ca}^{2+}(t) \circledast \delta\,(t - t_A) + B \times \mathrm{NE}(t) \circledast \delta(t - t_B)\end{aligned} \tag{3}$$

where t_A and t_B are global parameters representing, respectively, the delay between each of the neuronal variables (Ca^{2+} and NE) and HbT, while A and B are scalar weights that can vary across space (from pixel to pixel).

Because NE signals were highly correlated across brain regions (Extended Data Fig. 2k), we calculated the average NE signal across all pixels within the exposure. HbT, Ca^{2+} and NE signals were low-pass-filtered below 0.5 Hz using a sixth-order Butterworth filter. Next, HbT, Ca^{2+} and NE signals were normalized, pixelwise, to their s.d. in time to remove bias towards pixels with larger variance. To ease computational burden for the optimization algorithm, 32 × 32 spatial binning was applied to the HbT, Ca^{2+} and NE signals.

Similar to the variant IRF model, we simultaneously fit for two timing parameters (t_A and t_B in Eq. 3) and N regression weights (A and B in Eq. 3) in MATLAB (R2022a) using the 'fmincon' function. To allow t_A and t_B to vary continuously, we interpolated the delta function kernel between the two surrounding time bins. Timing parameter t_A was allowed to vary between 0 and 10 s and timing parameter t_B was allowed to vary between −5 and 10 s. Again, to extend to the original (not spatially binned) signals, we convolved the respective delta functions and parameter equal to t_A and t_B with our original Ca^{2+} and NE signals, respectively. This resulted in two time courses for Ca^{2+} and NE regressors. We then used linear regression, pixel by pixel, using the backslash operator in MATLAB to estimate the spatially varying weights (A and B) across pixels.

To evaluate the accuracy of this model across cortical space, we predicted the HbT time course for each pixel on the basis of Eq. 3 using the fitted global parameters t_A and t_B and the pixelwise parameters A and B. We then computed, pixel by pixel, the correlation between the predicted and experimentally obtained HbT using the entire duration of the data run (10 min).

Double IRF model

In our double IRF model, HbT is expressed as follows:

$$\mathrm{HbT}\,(t) = A \times \mathrm{IRF}_{\mathrm{Ca}^{2+}}(t)({t_0}^A, \tau_A) \circledast \mathrm{Ca}^{2+}\,(t) + B \times \mathrm{IRF}_{\mathrm{NE}}(t)({t_0}^B, \tau_B) \circledast \mathrm{NE}(t) \tag{4}$$

where IRF_{Ca2+} and IRF_{NE} are two stationary IRFs modeled with a single alpha function with respect to Ca^{2+} and NE, while A and B are scalar weights that can vary pixel to pixel.

As with the linear regression model, we low-pass-filtered the HbT signal below 0.5 Hz and normalized HbT, Ca^{2+} and NE signals, pixelwise, to their s.d. in time to remove bias toward pixels with larger variance. To ease computational burden for the optimization algorithm, 32 × 32 spatial binning was applied to the HbT, Ca^{2+} and NE signals. The IRF_{Ca2+} and IRF_{NE} kernels were modeled with a single alpha function with respect to Ca^{2+} and NE:

$$\mathrm{IRF}_{\mathrm{Ca}^{2+}}(t) = \left(\frac{t - {t_0}^A}{\tau_A}\right)^3 \times e^{-\frac{t - {t_0}^A}{\tau_A}} \tag{5}$$

$$\mathrm{IRF}_{\mathrm{NE}}(t) = \left(\frac{t - {t_0}^B}{\tau_B}\right)^3 \times e^{-\frac{t - {t_0}^B}{\tau_B}} \tag{6}$$

We chose an IRF kernel ranging from −5 to 10 s; however, ${t_0}^A$ was only allowed to vary between 0 and 10 s. A similar optimization algorithm was used as in the linear regression model to fit the global parameters ${t_0}^A$, τ_A, ${t_0}^B$ and τ_B and the pixelwise parameters A and B. Calculation of model performance remain the same as in the linear regression model.

Shuffled, HbO/HbR and unfiltered models

To further assess the linear regression and double IRF models, we repeated both models after circular shifting the NE signal. For each run, we circular shifted our NE signal and repeated both models for three separate shifts (25%, 50% and 75%). We averaged the resulting model performance maps, lag or IRF kernel and coefficient maps across all three shifts for each run.

Additionally, we repeated both models using the HbO and HbR signals in place of the HbT signal and we also repeated both models using the unfiltered HbT signal.

FC analysis

First, we low-pass-filtered the HbT signal below 0.5 Hz, normalized our Ca^{2+} and HbT time courses, pixelwise, to their s.d. in time to remove bias toward pixels with larger variance and parcellated the cortical surface on the basis of the mouse cortical Allen atlas[23] and calculated the average Ca^{2+} and HbT time course within each parcel. Then, we calculated seed correlation matrices for HbT and Ca^{2+} using a 30-s sliding window shifting every 6 s.

To relate dynamic FC to NE release, we computed the global NE signal (averaged across space) averaged within each sliding window. We then calculated the correlation between this NE time course and the dynamic Ca^{2+} and HbT connectivity (FC_{Ca++} and FC_{HbT}, respectively) between the MOs and SSp-ll regions. To compare FC_{Ca++} and FC_{HbT} spatial patterns, we calculated the correlation between the Ca^{2+} and HbT connectivity matrices for each time window. This resulted in a time course of correlation values, $r(FC_{Ca++}, FC_{HbT})$, which we then related to global NE release.

Additionally, to compare FC_{Ca++} and FC_{HbT} during periods of low and high NE release, we averaged the FC_{Ca++} and FC_{HbT} matrices during periods of low NE (global NE < 30th percentile) and during periods of high NE (global NE > 70th percentile) within each run, averaged across runs for each subject and then averaged across subjects.

For frequency-specific FC analysis, we first bandpass-filtered our Ca^{2+} or HbT signals using a sixth-order Butterworth filter in bands of <0.1, 0.1–0.5 and 0.5–5 Hz (MATLAB) and then repeated analysis.

To compare FC_{Ca++} and FC_{HbT} through time (Extended Data Fig. 9), we calculated the correlation between FC_{Ca++} and FC_{HbT} in time for each Allen atlas region pair. We then repeated this after regressing NE from the HbT signal using our linear regression model coefficients and after direct regression of the global NE signal from the HbT signal.

Spectral analysis

We performed all overall frequency spectrum calculations using the 'mtspectrumc' function of the Chronux toolbox[81] to calculate the Ca^{2+}, ACh, NE and HbT frequency spectra using nine tapers and a time bandwidth product of 5. This corresponds to a frequency resolution of 0.0167 Hz. All calculated spectra were normalized to their sum. We used the 'coherencyc' function (Chronux) to calculate the coherence and phase for Ca^{2+}/HbT, ACh/HbT and NE/HbT using nine tapers and a time bandwidth product of 5. Spectra were calculated for each pixel and then averaged across all pixels within the exposure.

Time-dependent spectral analysis (Extended Data Fig. 8) used the Morlet wavelets continuous wavelet transform to estimate spectrograms for the Ca^{2+} and HbT signals. First, we parcellated the cortical surface on the basis of the mouse cortical Allen atlas[23] and calculated the average Ca^{2+} and HbT time course within each parcel. We then calculated the spectrogram for each parcel using the Morlet wavelets approach with a full width at half maximum of 5 s and 300 frequency steps separated in a log scale. To define NE events, we first low-pass-filtered the global NE signal below 0.02 Hz. We then identified time points where the slope of the NE signal exceeded 0.05% per s and when the slope of the NE signal returned below 0.05% per s. We took the average of these two times and used it as the trial reference in Extended Data Fig. 8a–c. To compare periods of low and high NE release, we averaged the Ca^{2+} and HbT spectrums during periods of low NE (global NE < 30th percentile) and high NE (global NE > 70th percentile).

Lag cross-correlation and correlation analysis

To calculate lag cross-correlation between the optical signals, we calculated the lag cross-correlation per pixel and then averaged the cross-correlation function across all pixels within the exposure to generate a single, cortex-wide cross-correlation function.

To calculate the correlation between the optical signals and behavioral readouts, we first averaged our optical signals (Ca^{2+}, ACh, NE and HbT) across all pixels within the exposure and correlated them with the behavioral readouts (pupil diameter, whisking and movement).

Statistics and reproducibility

All data analysis and tests for statistical significance were calculated in MATLAB. Results were averaged across runs for each mouse and then averaged across mice. Error bars are shown as the standard error across subjects. When possible, statistics for each mouse are displayed. Differences among the global, SSp and variant IRF groups were tested using a paired, two-sided Wilcoxon signed-rank test (MATLAB 'signrank' function). Differences between groups containing separate subjects were tested using a two-sample, two-sided Kolmogorov–Smirnov test (MATLAB 'kstest2' function). *P* values are provided in the Source Data when not provided in the figure legends. The number of mice is given in figure legends and Supplementary Table 2.

For comparison of FC matrices, for each Allen region pair, we used a two-sided linear mixed-effects model to examine the relationship between connectivity for each region pair and level of NE (low versus high), while accounting for repeated measurements across multiple sessions per subject. Comparisons between low and high NE were performed separately for each region pair. Model fitting was performed using MATLAB's 'fitlme' function.

Runs where there were little fluctuations in pupil diameter were excluded. The investigators were not blinded to allocation during experiments and outcome assessment. No statistical method was used to predetermine sample size.

Reporting summary

Further information on research design is available in the Nature Portfolio Reporting Summary linked to this article.

Data availability

All data were uploaded to Distributed Archives for Neurophysiology Data Integration (https://doi.org/10.48324/dandi.001543/0.260130.1715)[82]. Source data are provided with this paper.

Code availability

All MATLAB code used to analyze wide-field data and to load the uploaded NWB files is available from GitHub (https://github.com/NIL-NeuroScience/Neuromodulation).

References

72. Dana, H. et al. Sensitive red protein calcium indicators for imaging neural activity. *eLife* **5**, e12727 (2016).
73. Chan, K. Y. et al. Engineered AAVs for efficient noninvasive gene delivery to the central and peripheral nervous systems. *Nat. Neurosci.* **8**, 1172–1179 (2017).
74. Goldey, G. J. et al. Removable cranial windows for long-term imaging in awake mice. *Nat. Protoc.* **9**, 2515–2538 (2014).
75. Kilic, K. et al. Chronic cranial windows for long term multimodal neurovascular imaging in mice. *Front. Physiol.* **11**, 612678 (2020).
76. Turner, K. L. et al. Neurovascular coupling and bilateral connectivity during NREM and REM sleep. *eLife* **9**, e62071 (2020).
77. Ma, Y. et al. Resting-state hemodynamics are spatiotemporally coupled to synchronized and symmetric neural activity in excitatory neurons. *Proc. Natl Acad. Sci. USA* **113**, E8463–E8471 (2016).
78. Kobat, D. et al. Deep tissue multiphoton microscopy using longer wavelength excitation. *Opt. Express* **17**, 13354–13364 (2009).
79. O'Shea, T. M. et al. Foreign body responses in mouse central nervous system mimic natural wound responses and alter biomaterial functions. *Nat. Commun.* **11**, 6203 (2020).
80. Stringer, C. et al. Spontaneous behaviors drive multidimensional, brainwide activity. *Science* **364**, eaav7893 (2019).
81. Bokil, H. et al. Chronux: a platform for analyzing neural signals. *J. Neurosci. Methods* **192**, 146–151 (2010).
82. Rauscher, B. et al. Neurovascular impulse response function (IRF) during spontaneous activity differentially reflects intrinsic neuromodulation across cortical regions. *DANDI* https://doi.org/10.48324/dandi.001543/0.260130.1715 (2026).

Acknowledgements

We thank Y. Li for providing the latest GRAB constructs. We thank A. Arkhipov, L.-H. Tsai and X. Han for helpful discussions and T. O'Shea for help with immunostainings. We gratefully acknowledge support from the National Institutes of Health (NIH; Brain Research Through Advancing Innovative Neurotechnologies (BRAIN) Initiative U19NS123717, BRAIN Initiative R01NS122742, R01DA050159 and T32NS136080), the Boston University Neurophotonics Center and the Boston University Kilachand Fund. B.C.R. was supported by a Ruth L. Kirschstein Predoctoral Fellowship F31NS145737 and Boston University Neurophotonics Center fellowship. P.R.D. was supported by a Ruth L. Kirschstein Predoctoral Fellowship F31NS118949. K.E.H. was supported by a Ruth L. Kirschstein Predoctoral Fellowship F31NS141509 and Boston University Neurophotonics Center CAN-DO award. N.X.C. was supported by a Garry Goldwater Undergraduate Fellowship and Boston University UROP award. P.F.B. was supported by the NIH (T32NS131178) and National Science Foundation Graduate Research Fellowship Program (2234657). The funders had no role in study design, data collection and analysis, decision to publish or preparation of the paper.

Author contributions

B.C.R. and N.F.-H., investigation, formal analysis, conceptualization, methodology, visualization, writing—original draft and writing—review and editing. S.K., formal analysis, methodology and writing—review and editing. P.R.D., methodology, software, writing—original draft and writing—review and editing. P.D.P., D.B. and P.F.B., formal analysis, conceptualization and writing—review and editing. N.X.C., F.A.F. and A.G., investigation, formal analysis and writing—review and editing. K.E.H., investigation, visualization, resources, writing—original draft and writing—review and editing. K.K., E.A.M. and J.X.J., resources and writing—review and editing. R.P.T. and S.G.K., investigation and writing—review and editing. J.P.G., M.L., D.K., M.E.H., L.D.L., E.P.S., D.A.B., L.T., G.M. and S.S., conceptualization, methodology, supervision and writing—review and editing. M.T., conceptualization, methodology, software, supervision, writing—original draft and writing—review and editing. A.D., conceptualization, funding acquisition, supervision, writing—original draft and writing—review and editing.

Competing interests

The authors declare no competing interests.

Additional information

Extended data is available for this paper at https://doi.org/10.1038/s41593-026-02239-7.

Supplementary information The online version contains supplementary material available at https://doi.org/10.1038/s41593-026-02239-7.

Correspondence and requests for materials should be addressed to Anna Devor.

Peer review information *Nature Neuroscience* thanks Alessandro Gozzi, Yen-Yu Shih, Valerio Zerbi and the other, anonymous, reviewer(s) for their contribution to the peer review of this work.

https://doi.org/10.1038/s41593-026-02239-7

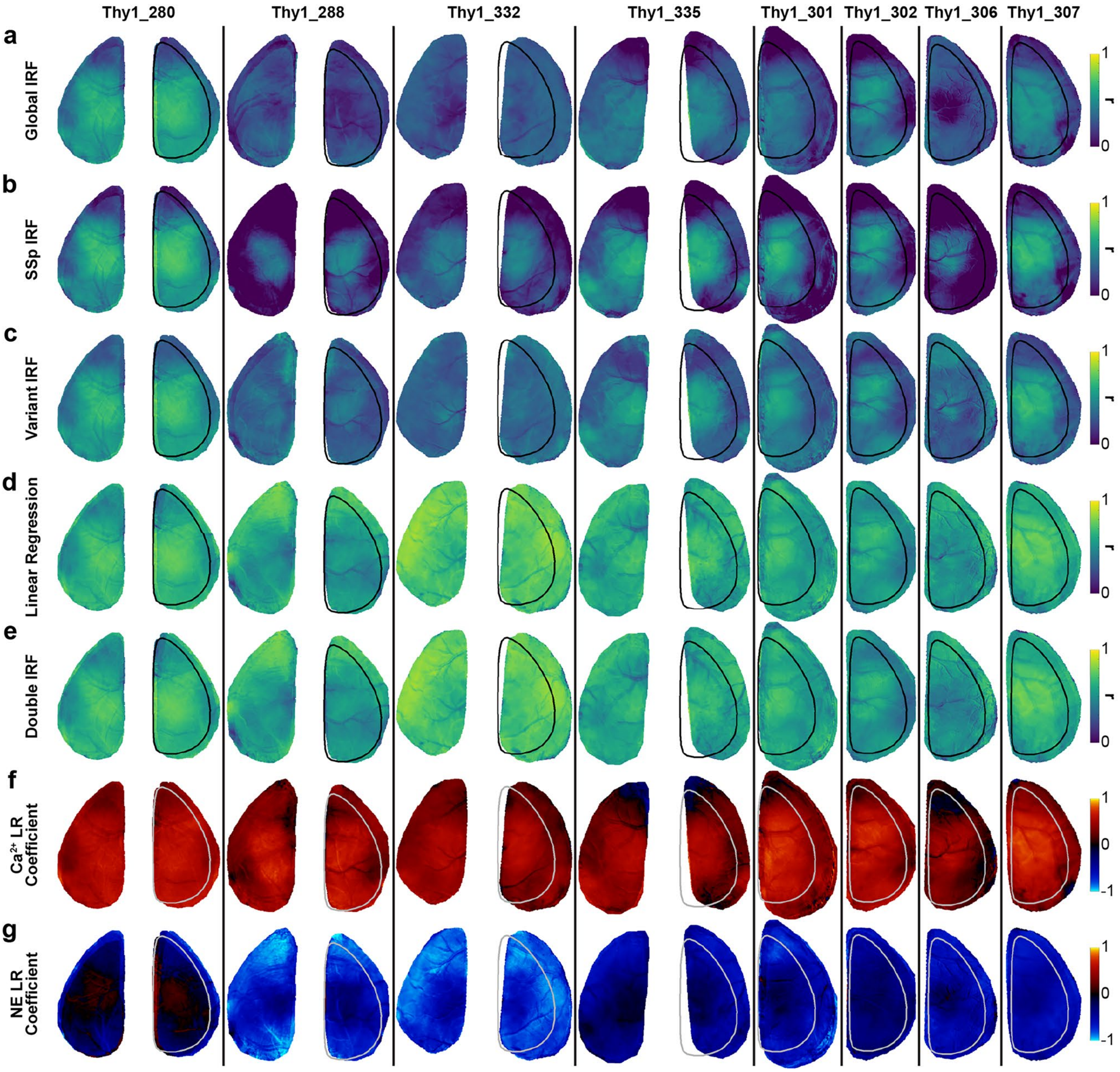

Extended Data Fig. 1 | Accuracy of the HbT models in the GRAB$_{NE}$ cohort. **a)** Maps of HbT prediction accuracy for the Global IRF model for each mouse in the GRAB$_{NE}$ cohort. The 'standard FOV' is outlined in black/gray. **b-e)** Same as (**a**) but for the SSp IRF, Variant IRF, Linear regression, and Double IRF model, respectively. **f-g)** Maps of the Ca^{2+} (**f**) and NE (**g**) coefficients (A and B, respectively) estimated in the Linear regression model for each mouse.

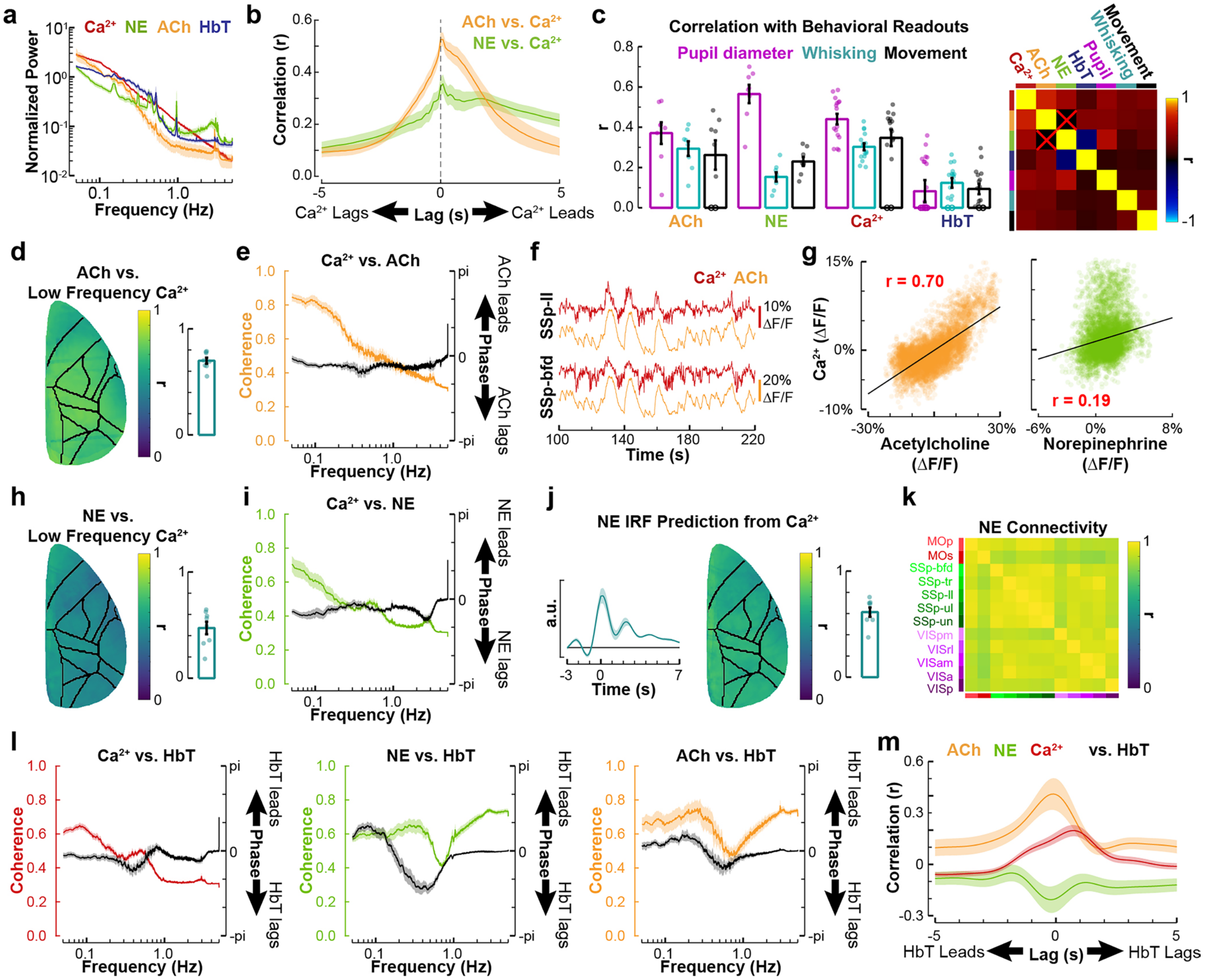

Extended Data Fig. 2 | Collinearity between optical measures and behavioral readouts. a) Normalized power spectra for Ca^{2+} (red), NE (green), ACh (orange), and HbT (blue; n = 16,8,8,16 subjects; mean ± SEM). **b)** Lag cross-correlation between ACh vs. Ca^{2+} (orange; n = 8 subjects; mean ± SEM) and NE vs. Ca^{2+} (green; n = 8 subjects; mean ± SEM). **c)** Left: average correlation between the eye pupil diameter (purple), whisking (cyan), and movement (black) with ACh, NE, Ca^{2+}, and HbT (n = 8,8,16,16 subjects; mean ± SEM; ***r*** = 0.37 ± 0.05, 0.29 ± 0.04, 0.26 ± 0.07, 0.56 ± 0.04, 0.15 ± 0.02, 0.23 ± 0.02, 0.44 ± 0.03, 0.30 ± 0.02, 0.35 ± 0.04, 0.08 ± 0.05, 0.12 ± 0.02, 0.09 ± 0.03). Each point represents an average across runs for one subject. Right: correlation matrix across all seven measurements. **d)** Correlation map between low pass filtered ACh and low pass filtered Ca^{2+} (< 0.5 Hz; n = 8 subjects). Space-averaged performance across subjects is shown on the right (n = 8 subjects; mean ± SEM; ***r*** = 0.70 ± 0.03). **e)** Coherence between Ca^{2+} and ACh (orange) and phase (black; n = 8 subjects; mean ± SEM). **f)** Example Ca^{2+} and ACh time-courses derived from the SSp-ll and SSp-bfd. **g)** Ca^{2+} averaged within the SSp-ll region plotted against the average ACh (left) and NE (right) within the same region for a single 10-min run. Correlation value displayed in red. **h)** Same as (**d**) but for NE vs. Ca^{2+} (n = 8 subjects; mean ± SEM; ***r*** = 0.47 ± 0.06). **i)** Same as (**e**) but for NE vs. Ca^{2+}. **j)** Direct IRF estimation using matrix division between NE and Ca^{2+} (left) and prediction accuracy map calculated as the correlation between the experimental and predicted NE (right; n = 8 subjects; mean ± SEM). Statistics across subjects is shown on the right (***r*** = 0.61 ± 0.04). **k)** Average connectivity matrix of NE showing the correlation across cortical regions (n = 8 subjects). **l)** Coherence along with phase lag between Ca^{2+} (left), NE (middle), and ACh (right) vs. HbT (n = 16,8,8 subjects, respectively; mean ± SEM). **m)** Lag cross-correlation between ACh (orange), NE (green), and Ca^{2+} (red) vs. HbT (n = 8,8,16 subjects, respectively; mean ± SEM).

https://doi.org/10.1038/s41593-026-02239-7

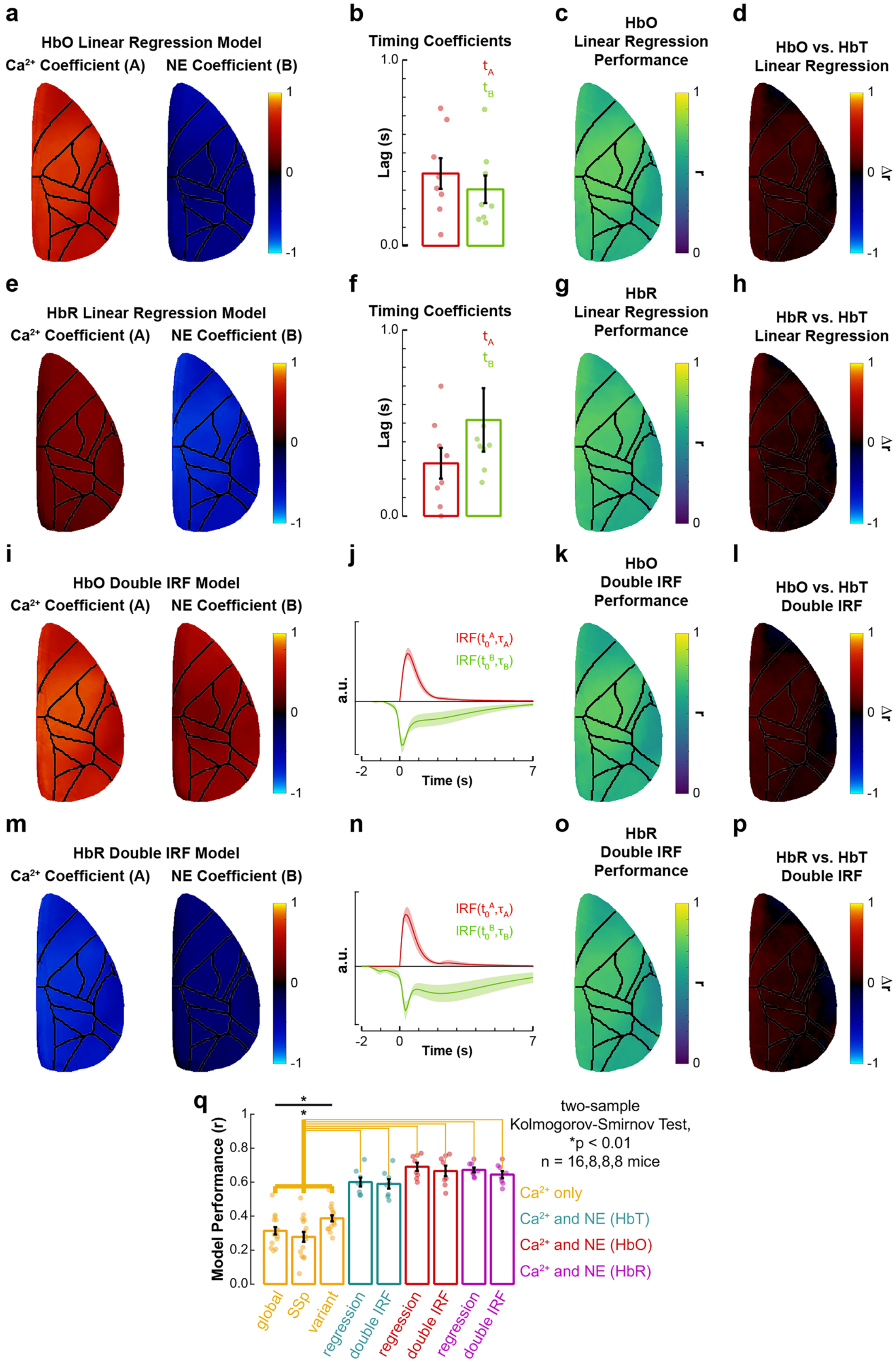

Extended Data Fig. 3 | See next page for caption.

Extended Data Fig. 3 | Linear Regression and Double IRF prediction models with respect to HbO and HbR. a) Maps of the weights, A (left) and B (right), in the Linear regression model for HbO (n = 8 subjects). **b)** HbO timing coefficients for Ca^{2+} and NE (t_A, t_B); each point corresponds to an average across runs for one subject (n = 8 subjects; mean ± SEM; $t_A = 0.39 \pm 0.08$, $t_B = 0.30 \pm 0.07$). **c)** Linear Regression model performance map quantified as the correlation between the experimental and predicted HbO (n = 8 subjects). **d)** Difference between HbO Linear Regression model performance and HbT Linear Regression model performance (n = 8 subjects). **e-h)** Same as (**a**-**d**) but for HbR. For (**f**), $t_A = 0.28 \pm 0.08$, $t_B = 0.52 \pm 0.17$. **i, k, l, m, o, p)** Same as (**a**, **c**, **d**, **e**, **g**, **h**) but for the Double IRF model. **j, n)** Estimated IRF_{Ca2+} and IRF_{NE} for the HbO and HbR model (n = 8 subjects; mean ± SEM). **q)** Side-by-side model comparison. For each subject and model, the model performance (***r***) was averaged across space. Each point represents one subject (*p < 0.01 two-sample, two-sided Kolmogorov-Smirnov Test; mean ± SEM; ***r*** = 0.32 ± 0.02, 0.29 ± 0.03, 0.39 ± 0.02, 0.60 ± 0.03, 0.59 ± 0.03, 0.69 ± 0.02, 0.67 ± 0.03, 0.67 ± 0.01, 0.65 ± 0.02; n = 16 subjects for Global, SSp, and Variant models; n = 8 subjects for Double IRF and Linear regression models). P-values are provided in figure source data.

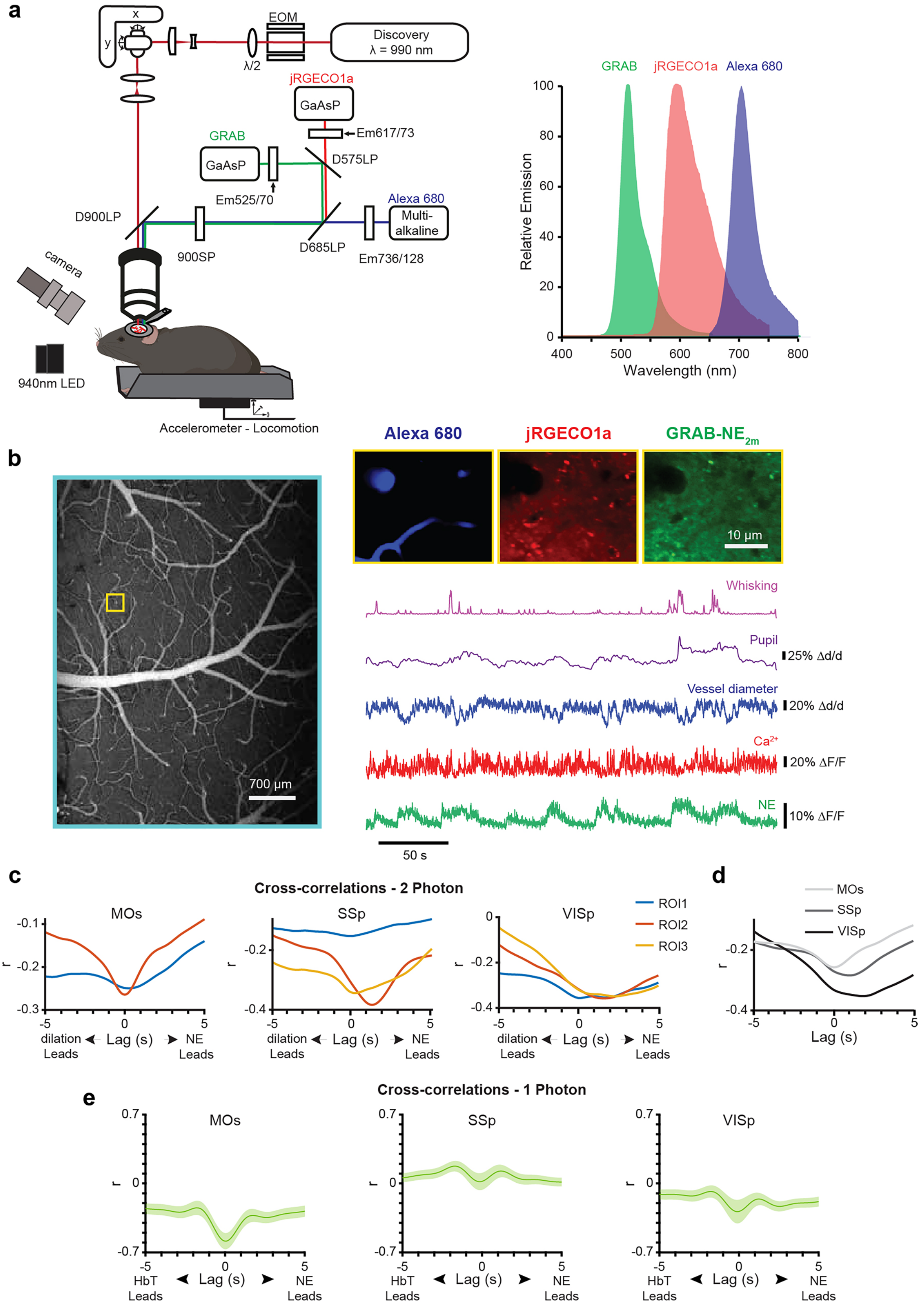

Extended Data Fig. 4 | See next page for caption.

Extended Data Fig. 4 | Two-photon imaging of Ca^{2+}, NE, and arteriolar diameter. a) Imaging setup depicts Ti:sapph laser set to 990 traveling through an electro-optic modulator (EOM) to excite $GRAB_{NE}$, jRGECO1a and Alexa 680; D900LP, D685LP and D575LP—long-pass dichroic mirrors with a cutoff at 900, 685 and 575 nm, respectively; GaAsP and multialkaline—PMT tubes; 900SP—short-pass optical filter with a cutoff at 900 nm; Em525/70, Em617/70, Em736/128—bandpass emission filters. Absorption plot at the top right indicates the emission spectra of our desired fluorophores. **b)** Left: An example average intensity projection of a low magnification image stack across the top 300 µm showing the vasculature labeled with Alexa 680. Yellow rectangle indicates the ROI chosen for imaging of brain activity. Right: A field of view 170 µm below the cortical surface with a diving arteriole labeled with Alexa 680(blue), neurons labeled with jRGECO1a (red), and $GRAB_{NE}$ (green). Time-courses at the bottom show spontaneous activity acquired at 10 Hz. **c)** Cross-correlation of the NE signal and arteriolar diameter for different arteries (ROIs) across three cortical regions: MOs, SSp and VISp. **d)** Average across ROIs for the three cortical regions. **e)** Cross-correlation of the NE signal and HbT derived from mesoscale imaging (n = 8 subjects; mean ± SEM).

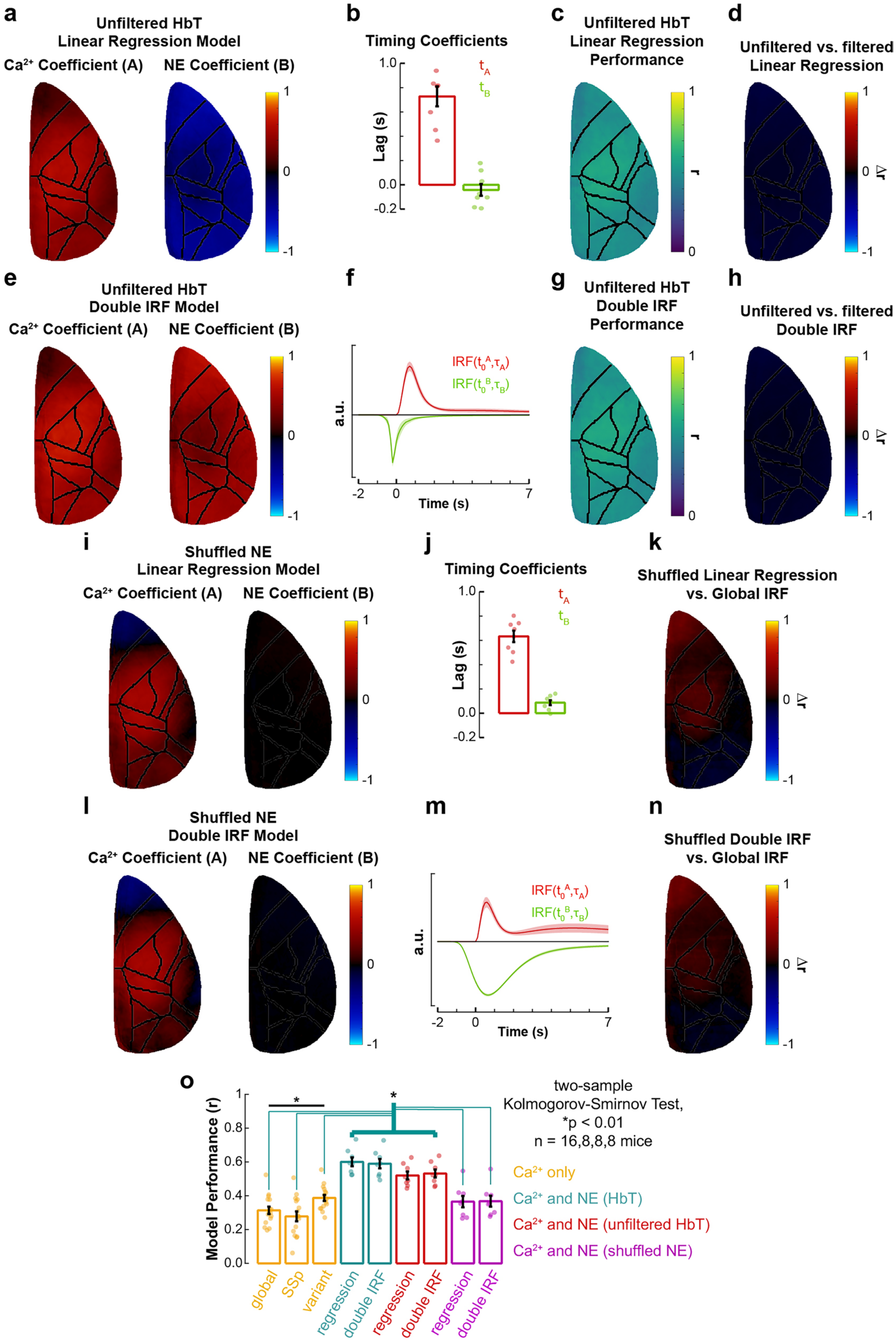

Extended Data Fig. 5 | See next page for caption.

Extended Data Fig. 5 | Effects of HbT filtering and NE reshuffling. a) Maps of the weights, A (left) and B (right), in the Linear regression model using unfiltered HbT (n = 8 subjects). **b)** Timing coefficients for Ca^{2+} and NE ($\boldsymbol{t_A}$, $\boldsymbol{t_B}$) for each subject using unfiltered HbT; each dot shows an average across runs for one subject (n = 8 subjects; mean ± SEM; $t_A = 0.73 \pm 0.08$, $t_B = -0.04 \pm 0.05$). **c)** Linear Regression model performance map quantified as the correlation between experimental and predicted HbT using unfiltered HbT (n = 8 subjects). **d)** Difference between unfiltered and filtered Linear Regression model performance (n = 8 subjects). **e, g, h)** Same as (**a**, **c**, **d**) but for the Double IRF model. **f)** Estimated IRF_{Ca2+} and IRF_{NE} using unfiltered HbT (n = 8 subjects; mean ± SEM). **i)** Maps of the weights, A (left) and B (right), in the Linear regression model after shuffling the NE data (n = 8 subjects). **j)** Timing coefficients for Ca^{2+} and NE ($\boldsymbol{t_A}$, $\boldsymbol{t_B}$) for each subject after shuffling NE; each dot shows an average across runs for one subject (n = 8 subjects; mean ± SEM; $t_A = 0.63 \pm 0.05$, $t_B = 0.09 \pm 0.02$). **k)** Difference between shuffled NE Linear Regression model performance and Global IRF model performance (n = 8 subjects). **l, n)** Same as (**i**, **k**) but for the Double IRF model. **m)** Estimated IRF_{Ca2+} and IRF_{NE} after shuffling NE (n = 8 subjects; mean ± SEM). **o)** Side-by-side model comparison. For each subject and model, the model performance (***r***) was averaged across space. Each point represents one subject (*$p < 0.01$ two-sample, two-sided Kolmogorov-Smirnov Test; mean ± SEM; ***r*** = 0.32 ± 0.02, 0.29 ± 0.03, 0.39 ± 0.02, 0.60 ± 0.03, 0.59 ± 0.03, 0.52 ± 0.02, 0.53 ± 0.02, 0.37 ± 0.03, 0.37 ± 0.03 for the Global, SSp, and variant IRF models, the Linear Regression and Double IRF models, the unfiltered Linear Regression and Double IRF models, and the shuffled Linear Regression and Double IRF models; n = 16 subjects for the Global, SSp, and variant IRF models n = 8 subjects for all models using NE). P-values are provided in figure source data.

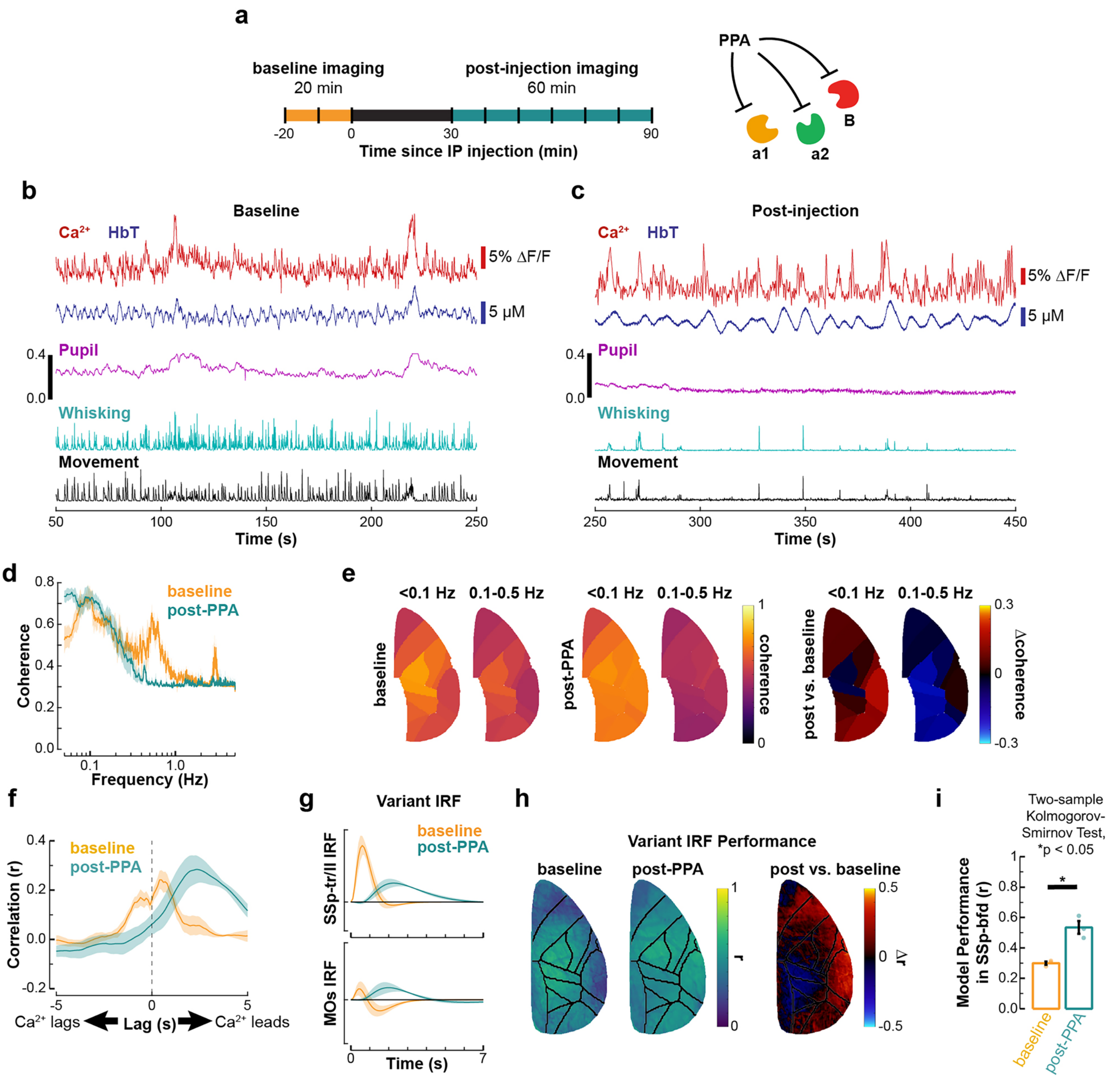

Extended Data Fig. 6 | Blockade of a- and b-adrenergic receptors. **a)** Schematic of the experimental paradigm. A cocktail of prazosin, propranolol, and atipamezole (PPA) was delivered IP. **b-c)** Example Ca^{2+} and HbT time courses along with behavior readouts recorded during the baseline (pre-PPA, b) and post-injection (post-PPA, c). **d)** Coherence between Ca^{2+} and HbT pre- (orange) and post-PPA (cyan) coherence (n = 3 subjects; mean ± SEM). **e)** Left: Coherence in the <0.1 Hz and 0.1-0.5 Hz frequency band for each cortical region comparing pre- and post-PPA. Right: difference between the pre- and post-PPA (averaged across 3 subjects). **f)** Lag cross-correlation between Ca^{2+} and HbT comparing pre- (orange) and post-PPA (cyan; averaged across 3 subjects; mean ± SEM). **g)** Estimated IRF$_{Ca2+}$ using the Variant IRF model from SSp-tr and SSp-ll (top) and MOs (bottom) comparing pre- (orange) and post-PPA (cyan; averaged across 3 subjects; mean ± SEM). **h)** Accuracy of the Variant IRF model comparing pre- and post-PPA along with the difference between the two (n = 3 subjects). **i)** Average Variant IRF performance pre- and post-PPA (orange and cyan, respectively) in SSp-bfd. Each dot shows an average across runs for one subject (*p < 0.05 two-sample, two-sided Kolmogorov-Smirnov Test; n = 3 subjects; mean ± SEM; **r** = 0.30 ± 0.01, 0.53 ± 0.04 for pre- and post-PPA, respectively, **p** = 3.3e-2).

https://doi.org/10.1038/s41593-026-02239-7

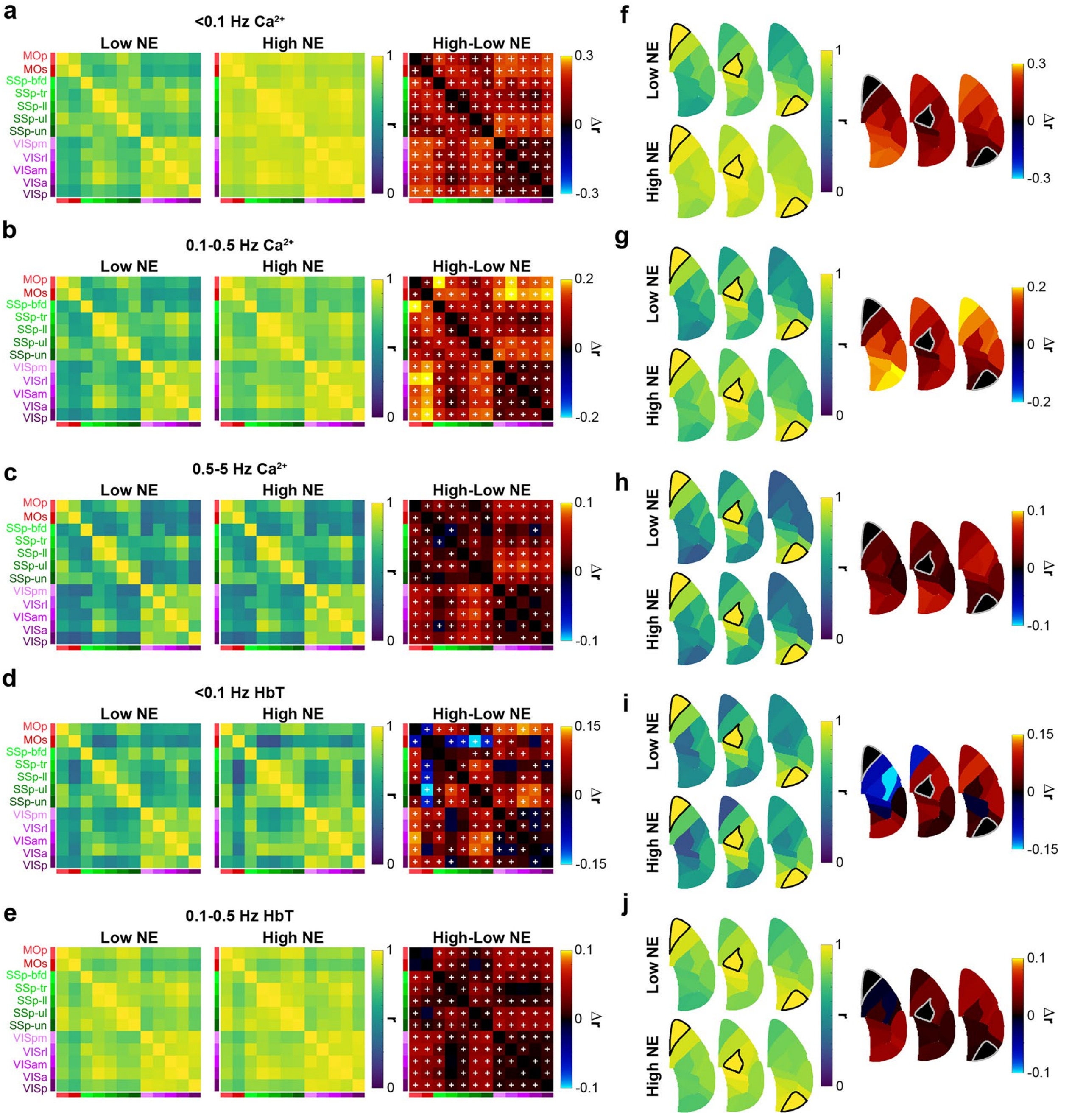

Extended Data Fig. 7 | Comparison of FC results for high and low frequency Ca^{2+} activity and HbT. a) Low frequency (< 0.1 Hz) Ca^{2+} connectivity matrices, averaged across subjects, comparing connectivity during low NE (< 30th percentile; left) and high NE (> 70th percentile; middle). Right: Difference between the high and low NE ('+' indicates $p < 0.05$, two-sided linear mixed-effects model, comparisons between low and high NE were performed separately for each region pair, n = 123 sessions, 8 subjects). P-values are provided in figure source data. **b-c)** Same as (**a**) but for 0.1-0.5 Hz and 0.5-5 Hz frequency bands. **d-e)** Same as (**a**-**b**) but for HbT. **f)** Low frequency (< 0.1 Hz) Ca^{2+} seed correlation maps, averaged across subjects, comparing connectivity during low NE and high NE for MOs, SSp-ll, and VISp regions (n = 8 subjects). **g-h)** Same as (**f**) but for 0.1-0.5 Hz and 0.5-5 Hz frequency bands. **i-j)** Same as (**f**-**g**) but for HbT.

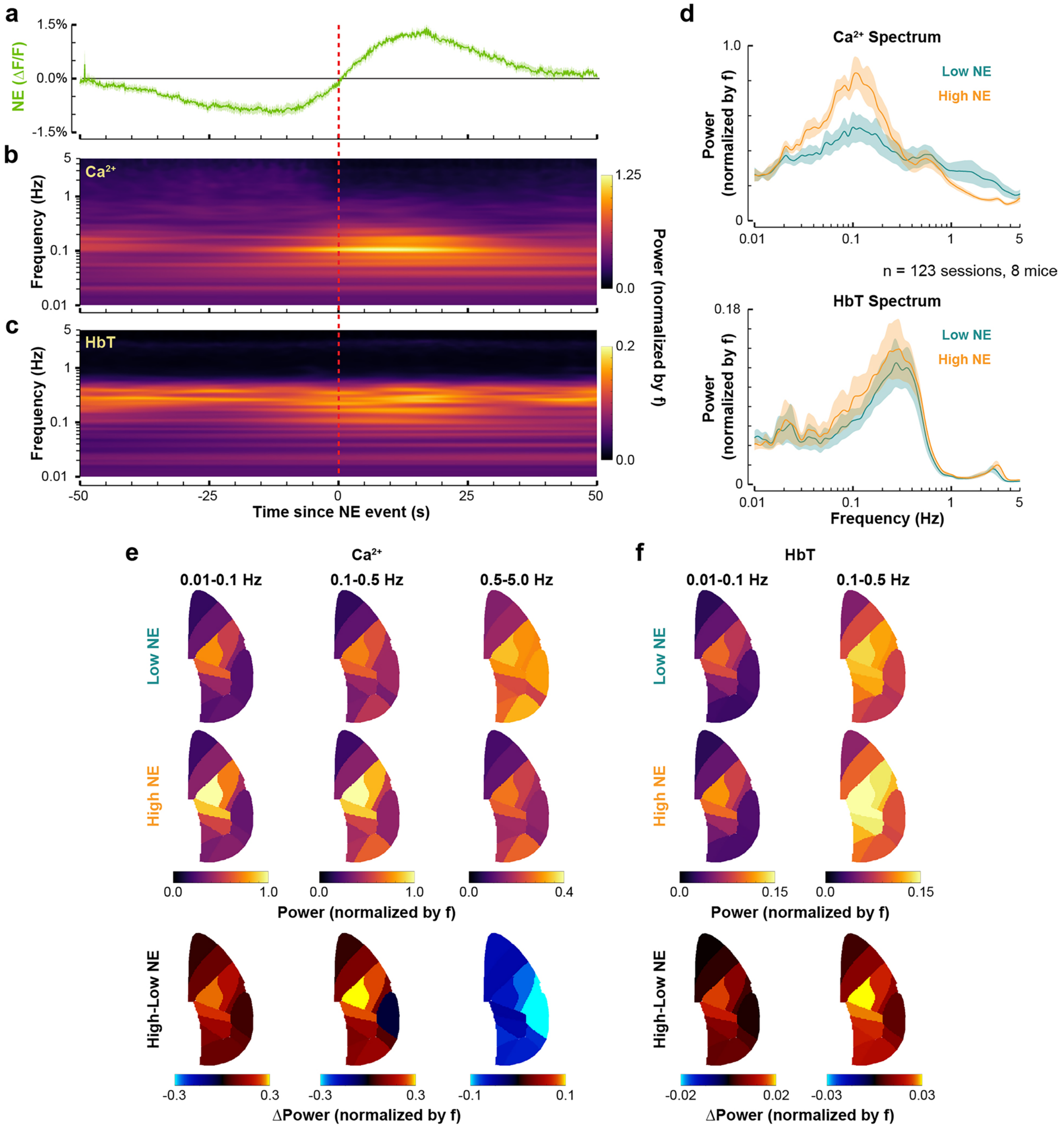

Extended Data Fig. 8 | Spectral analysis of Ca^{2+} and HbT during low and high NE. a) The average of detected global NE "events" (see **Methods**) (n = 301 events accumulated from 8 subjects; mean ± SEM). **b)** Averaged event-triggered global Ca^{2+} spectrogram corresponding to the NE events from (**a**) (n = 301 events, 8 subjects). The power is multiplied by frequency to correct for the 1/f relationship. **c)** Same as (**b**) but for global HbT (n = 301 events, 8 subjects). **d)** Comparison between subject-averaged, global Ca^{2+} and HbT spectra (top and bottom, respectively) during periods of low NE (< 30th percentile; cyan) and high NE (> 70th percentile; orange) (n = 8 subjects; mean ± SEM). The power is multiplied by frequency to correct for the 1/f relationship. **e)** Maps of the average Ca^{2+} spectral power (corrected for 1/f) during periods of low (top) and high (middle) NE. Bottom: The difference between high and low NE; n = 8 subjects). **f)** Same as (**e**) but for HbT (n = 8 subjects).

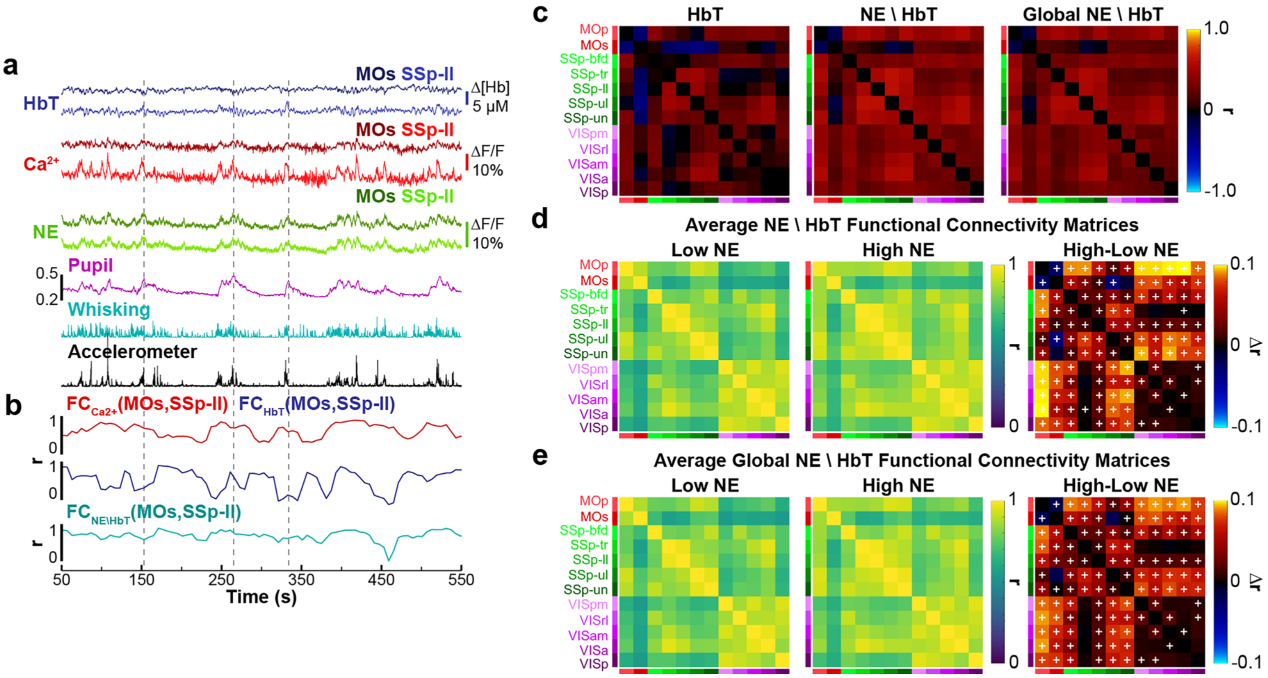

Extended Data Fig. 9 | Regression of NE from HbT increases the similarity between FC_{Ca} and FC_{HbT}. **a)** Excerpt from Fig. 3a: Example Ca^{2+}, NE, and HbT time-courses derived from two cortical regions, MOs and SSp-ll, along with behavior readouts. The dashed vertical lines indicate several NE peaks to facilitate visual inspection. **b)** Top: Excerpt from Fig. 3b**:** Dynamic functional connectivity between MOs and SSp-ll for Ca^{2+} (red) and HbT (blue) computed as the correlation between the respective time-courses using a 30-s sliding window. Bottom: Dynamic functional connectivity between MOs and SSp-ll for HbT after regression of the NE signal using the Linear regression model weights and lag. **c)** Left: Subject-averaged correlation between Ca^{2+} and HbT connectivity time courses (see **Methods**). Middle: the same after regression of region-specific NE signal from HbT using the Linear regression model. Right: the same as the left panel after direct regression of global NE from HbT (n = 8 subjects, n = 123 sessions, 8 subjects). **d)** Average HbT connectivity matrices comparing connectivity during low NE (< 30th percentile; left) and high NE (> 70th percentile; middle) after regression of region-specific NE signal using the Linear regression model. Right: Difference between the high and low NE ('+' indicates $p < 0.05$, two-sided linear mixed-effects model, comparisons between low and high NE were performed separately for each region pair, n = 123 sessions, 8 subjects). P-values are provided in figure source data. **e)** Same as (**d**) but regressing global NE from HbT.

https://doi.org/10.1038/s41593-026-02239-7

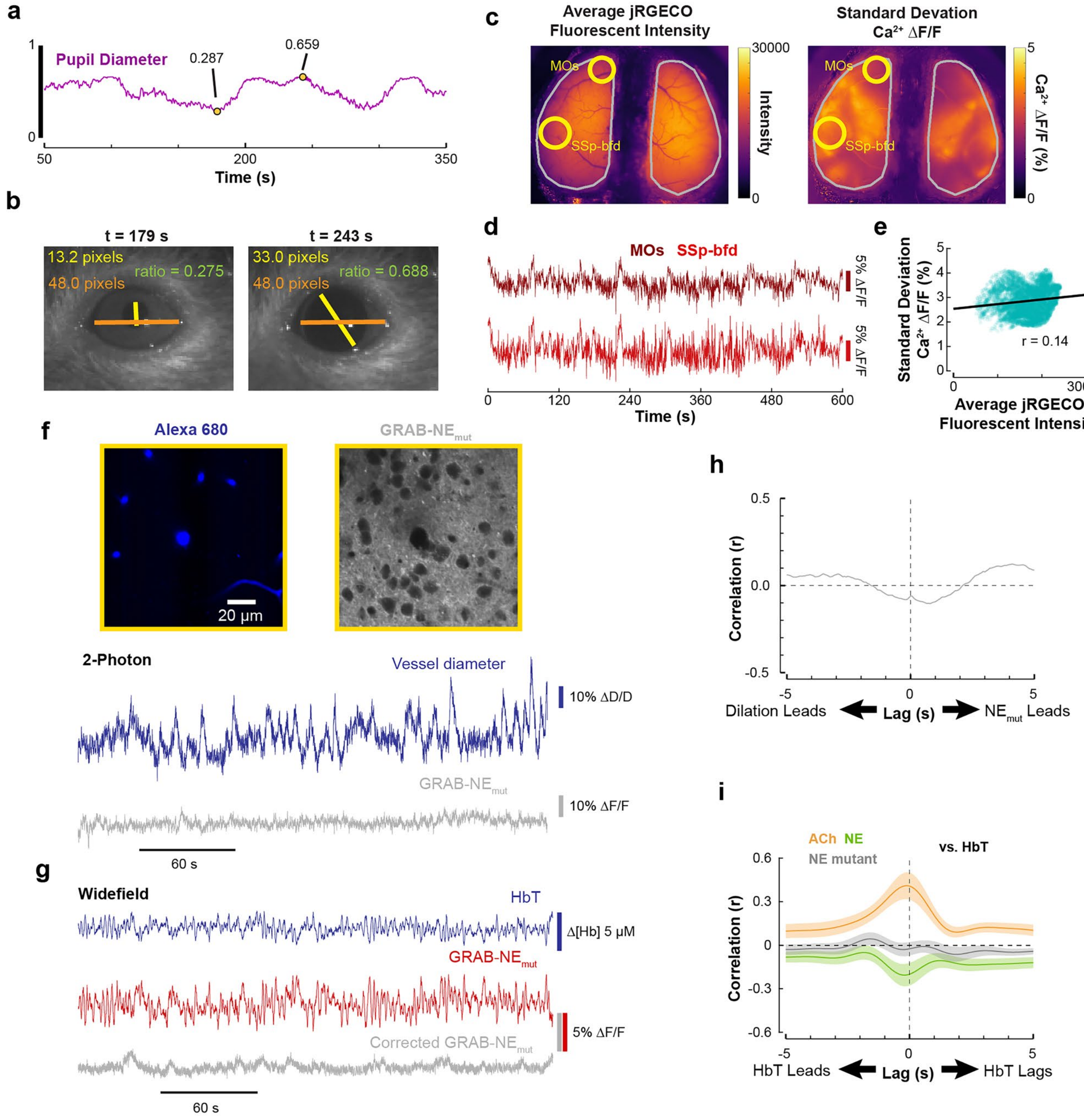

Extended Data Fig. 10 | The eye pupil diameter measurement, illumination, and hemodynamic correction. a-b) Agreement between automated and manual eye pupil measurements. Example time-course of estimated pupil diameter using the algorithm described in **Methods** (**a**) and manual eye pupil measurement (**b**) corresponding to the time points marked in (**a**). The video frames in (**b**) (179 and 243 s) show manual annotations of the eye and eye pupil diameter and the calculated ratio. **c)** Variability in Ca^{2+} signal amplitude does not follow variation in the illumination intensity. Left: An example map of the average raw jRGECO fluorescent intensity (F) for a single run reflecting variation in the illumination intensity. Right: A map of the standard deviation of the Ca^{2+} ΔF/F signal for the same run. **d)** Example time courses of Ca^{2+} ΔF/F from the MOs and SSp-bfd. **e)** The pixel-by-pixel standard deviation of the Ca^{2+} ΔF/F signal across time plotted against the average raw jRGECO fluorescent intensity for the same pixels within the exposure outlined in (**c**). **f)** Top: A 2-photon imaging field of view 230 µm below the cortical surface with a diving arteriole labeled with Alexa 680 (blue) and GRAB$_{\text{NE-mutant}}$ (gray). Time-courses at the bottom show spontaneous activity acquired at ~15 Hz. **g)** Example widefield HbT (blue), uncorrected GRAB$_{\text{NE-mutant}}$ signal (red), and corrected GRAB$_{\text{NE-mutant}}$ signal (gray) time-courses from SSp-ll. **h)** Average cross-correlation function between 2-photon GRAB$_{\text{NE-mutant}}$ vs. vessel diameter for the imaging session shown in (**f**). **i)** Subject-averaged cross-correlation functions between widefield GRAB$_{\text{ACh}}$, GRAB$_{\text{NE}}$, and GRAB$_{\text{NE-mutant}}$ vs. HbT (n = 8,8,3 subjects, respectively; mean ± SEM).

nature portfolio

Corresponding author(s): Anna Devor

Last updated by author(s): 01/30/2026

Reporting Summary

Nature Portfolio wishes to improve the reproducibility of the work that we publish. This form provides structure for consistency and transparency in reporting. For further information on Nature Portfolio policies, see our Editorial Policies and the Editorial Policy Checklist.

Statistics

For all statistical analyses, confirm that the following items are present in the figure legend, table legend, main text, or Methods section.

n/a	Confirmed	
☐	☒	The exact sample size (*n*) for each experimental group/condition, given as a discrete number and unit of measurement
☐	☒	A statement on whether measurements were taken from distinct samples or whether the same sample was measured repeatedly
☐	☒	The statistical test(s) used AND whether they are one- or two-sided *Only common tests should be described solely by name; describe more complex techniques in the Methods section.*
☒	☐	A description of all covariates tested
☒	☐	A description of any assumptions or corrections, such as tests of normality and adjustment for multiple comparisons
☐	☒	A full description of the statistical parameters including central tendency (e.g. means) or other basic estimates (e.g. regression coefficient) AND variation (e.g. standard deviation) or associated estimates of uncertainty (e.g. confidence intervals)
☐	☒	For null hypothesis testing, the test statistic (e.g. *F*, *t*, *r*) with confidence intervals, effect sizes, degrees of freedom and *P* value noted *Give P values as exact values whenever suitable.*
☒	☐	For Bayesian analysis, information on the choice of priors and Markov chain Monte Carlo settings
☒	☐	For hierarchical and complex designs, identification of the appropriate level for tests and full reporting of outcomes
☐	☒	Estimates of effect sizes (e.g. Cohen's *d*, Pearson's *r*), indicating how they were calculated

Our web collection on statistics for biologists contains articles on many of the points above.

Software and code

Policy information about availability of computer code

Data collection	Widefield imaging was done on a custom-built system operated with the Solis software (Andor). Acquisition was done using custom MATLAB-scripts which utilize a National Instruments DAQ system to control LED triggers and record accelerometer readouts. Two photon imaging was performed with a Discovery 2-photon laser scanning microscopy system from Bruker Fluorescence Microscopy operated with PrairieView.
Data analysis	Custom MATLAB (Mathworks, v2022a) code, built-in MATLAB functions, and the Chronux toolbox (Bokil et al. 2010) were used for data analysis. Algorithms used include convolution and deconvolution using custom MATLAB scripts, regression analysis using custom MATLAB scripts, Student's t test (ttest2.m), and multitaper method for spectral analysis (mtspectrumc.m and coherencyc.m from the Chronux toolbox). All code used to analyze widefield data is available at: https://github.com/NIL-NeuroScience/Neuromodulation. Adobe Illustrator (26.3.1) was used for figure preparation.

For manuscripts utilizing custom algorithms or software that are central to the research but not yet described in published literature, software must be made available to editors and reviewers. We strongly encourage code deposition in a community repository (e.g. GitHub). See the Nature Portfolio guidelines for submitting code & software for further information.

Data

Policy information about availability of data

All manuscripts must include a data availability statement. This statement should provide the following information, where applicable:

- Accession codes, unique identifiers, or web links for publicly available datasets
- A description of any restrictions on data availability
- For clinical datasets or third party data, please ensure that the statement adheres to our policy

The data that supports the findings of this study can be accessed through DANDI archive using the following link: https://dandiarchive.org/dandiset/001543/.

Research involving human participants, their data, or biological material

Policy information about studies with human participants or human data. See also policy information about sex, gender (identity/presentation), and sexual orientation and race, ethnicity and racism.

Reporting on sex and gender	N/A
Reporting on race, ethnicity, or other socially relevant groupings	N/A
Population characteristics	N/A
Recruitment	N/A
Ethics oversight	N/A

Note that full information on the approval of the study protocol must also be provided in the manuscript.

Field-specific reporting

Please select the one below that is the best fit for your research. If you are not sure, read the appropriate sections before making your selection.

☒ Life sciences ☐ Behavioural & social sciences ☐ Ecological, evolutionary & environmental sciences

For a reference copy of the document with all sections, see nature.com/documents/nr-reporting-summary-flat.pdf

Life sciences study design

All studies must disclose on these points even when the disclosure is negative.

Sample size	Sample size of mice with similar fluorescent sensors for neuronal Ca2+ activity and hemodynamic imaging was determined empirically based on previous study samples (Shahsavarani et al. 2023. "Cortex-wide neural dynamics predict behavioral states and provide a neural basis for resting-state dynamic functional connectivity". Cell Reports, 42, 112527) and aimed to minimize the number of live animals.
Data exclusions	Runs which contained no significant dynamics in pupil diameter or NE release were excluded.
Replication	Results were verified between animals.
Randomization	No randomization was used in this study. All mice received GRAB virus injections and were subject to the same conditions and tests.
Blinding	Experimenters were not blind to the imaging because all mice were subject to the same conditions.

Reporting for specific materials, systems and methods

We require information from authors about some types of materials, experimental systems and methods used in many studies. Here, indicate whether each material, system or method listed is relevant to your study. If you are not sure if a list item applies to your research, read the appropriate section before selecting a response.

Materials & experimental systems

n/a	Involved in the study	
☐	☒	Antibodies
☒	☐	Eukaryotic cell lines
☒	☐	Palaeontology and archaeology
☐	☒	Animals and other organisms
☒	☐	Clinical data
☒	☐	Dual use research of concern
☒	☐	Plants

Methods

n/a	Involved in the study	
☒	☐	ChIP-seq
☒	☐	Flow cytometry
☒	☐	MRI-based neuroimaging

Antibodies

Antibodies used	Anti-GFP (1:1000; Abcam, ab13970).
Validation	Anti-GFP: This antibody has been extensively validated by the manufacturer (Abcam). CiteAb lists over 4,500 citations.

Animals and other research organisms

Policy information about studies involving animals; ARRIVE guidelines recommended for reporting animal research, and Sex and Gender in Research

Laboratory animals	For this study Thy1_jRGECO1a mice from the GP8.20 line under a C57BL/6 background were used. Mice were typically between 4 and 6 months old when imaged.
Wild animals	This study did not involve wild animals.
Reporting on sex	In this study, 5 male mice and 15 female mice were used. Sex was not considered in analysis or study design.
Field-collected samples	This study did not involve samples collected from the field.
Ethics oversight	All experimental procedures were performed in accordance with the guidelines established by the Boston University Institutional Animal Care and Use Committee

Note that full information on the approval of the study protocol must also be provided in the manuscript.

Plants

Seed stocks	N/A
Novel plant genotypes	N/A
Authentication	N/A